

Multifunctional Bioactive Dual-Layered Nanofibrous Matrix for Effective Breast Cancer Therapy and Enhanced Wound Healing

Sungyun Kim, Da In Jeong, Mrinmoy Karmakar, Ji-Won Huh, Eun-Hye Hong, Dae-Joon Kim, Hyun-Jeong Ko, Hyun-Jong Cho,* and Ki-Bum Lee*

Surgical resection is the primary treatment for triple-negative breast cancer (TNBC). Post-operative complications, including tumor recurrence and bacterial infections, hinder complete remission and long-term recovery. To address these challenges, a multifunctional bioactive dual-layered nanofibrous matrix (MBDL-NanoMat) featuring adaptive shape control, excellent wound adherence, tunable drug release profiles, and superior biocompatibility for post-surgical applications is developed. The MBDL-NanoMat comprises a hydrophilic (HyPhil) layer and a hydrophobic (HyPhob) layer, offering distinct functionalities. The HyPhil layer, electrospun with gelatin and copper peroxide nanoparticles (Cu NPs), rapidly releases Cu NPs to induce anticancer effects through chemodynamic therapy (CDT), ferroptosis, and cuproptosis along with antibacterial action. Near-infrared laser irradiation enhances therapeutic efficacy through photothermal therapy (PTT). The HyPhob layer ensures prolonged therapeutic effects by releasing therapeutic molecules, such as rapamycin, enabling sustained chemotherapy (CT) and antibacterial activity. This synergistic therapeutic system integrates multiple mechanisms—CT, CDT, PTT, ferroptosis, and cuproptosis—suppressing tumor recurrence and accelerating wound healing. Preclinical results demonstrated enhanced angiogenesis, collagen deposition, and dermal regeneration without systemic safety. In short, the MBDL-NanoMat platform offers a unique advantage in post-surgical TNBC care by simultaneously targeting tumor recurrence and facilitating wound healing. Further investigation of this platform can significantly improve oncological and regenerative medicine strategies.

1. Introduction

Triple-negative breast cancer (TNBC) is a subtype of breast cancer defined by the absence of estrogen receptors, progesterone receptors, and human epidermal growth factor receptor 2.^[1] This aggressive subtype comprises 15–20% of all breast cancers and poses significant therapeutic challenges due to its poor response to conventional treatments and highly invasive nature. Furthermore, the limited availability of targeted therapies often leads to surgery being the primary treatment option.^[2] Following TNBC surgery, various approaches have been used for treating the surgical site, such as wound dressing, autologous tissue grafts, and stem cell therapy (Figure 1A).^[3] However, achieving complete resection can be challenging, and residual cancer cells can lead to tumor resurgence (Figure 1A).^[4] Moreover, bacterial infections following surgery can disrupt the natural wound healing and tissue regeneration processes, leading to prolonged hospital stays and elevated healthcare costs (Figure 1A).^[5] Thus, it is imperative to develop multifunctional scaffolds that can target cancer treatment while promoting

S. Kim, D. I. Jeong, M. Karmakar, J.-W. Huh, E.-H. Hong, D.-J. Kim, H.-J. Ko, H.-J. Cho
Department of Pharmacy
Kangwon National University
Chuncheon, Gangwon 24341, Republic of Korea
E-mail: hjcho@kangwon.ac.kr

S. Kim, K.-B. Lee
Department of Chemistry and Chemical Biology, Rutgers
The State University of New Jersey
123 Bevier Road, Piscataway, NJ 08854, USA
E-mail: kblee@rutgers.edu

K.-B. Lee
Department of Regulatory Science Graduate School
Kyung Hee University
Seoul 02447, Republic of Korea

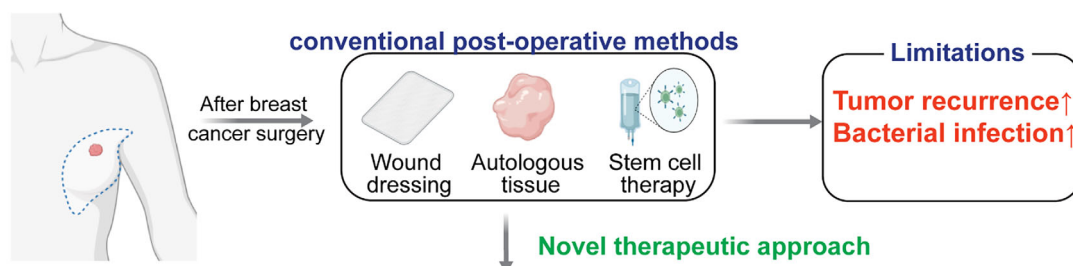
K.-B. Lee
Institute of Regulatory Innovation through Science (IRIS)
Kyung Hee University
Seoul 02447, Republic of Korea

The ORCID identification number(s) for the author(s) of this article can be found under <https://doi.org/10.1002/smll.202500717>

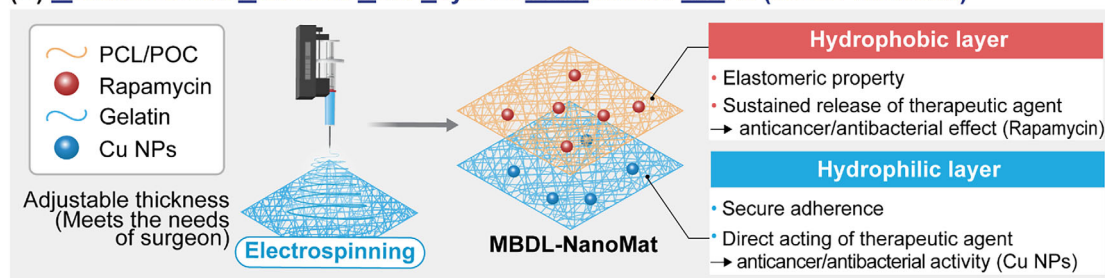
© 2025 The Author(s). Small published by Wiley-VCH GmbH. This is an open access article under the terms of the [Creative Commons Attribution-NonCommercial-NoDerivs](#) License, which permits use and distribution in any medium, provided the original work is properly cited, the use is non-commercial and no modifications or adaptations are made.

DOI: 10.1002/smll.202500717

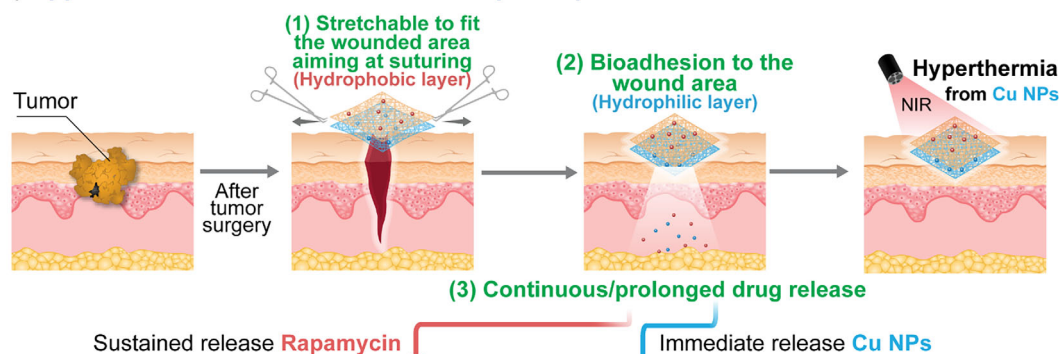
(A) Limitation of current treatment after breast cancer surgery



(B) Multifunctional Bioactive Dual-Layered Nanofibrous Matrix (MBDL-NanoMat)



(C) Application of the MBDL-NanoMat for post-operative treatment of breast cancer



(D) Strategy for multiple anticancer/antibacterial functions for complete wound healing

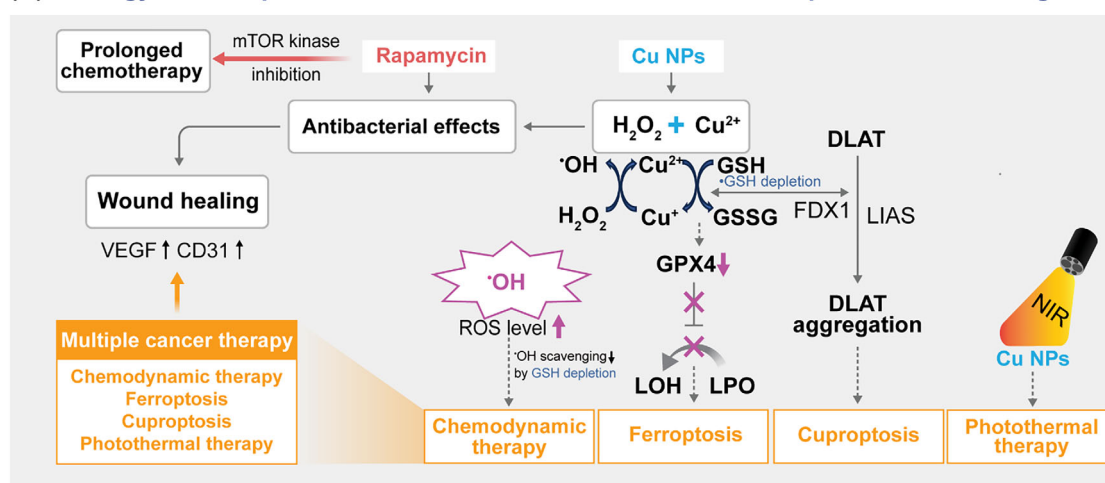


Figure 1. Illustration of the designed MBDL-NanoMat for adjuvant cancer therapy and wound healing application. A) Schematic diagram of current limitations in breast cancer surgery. B) The manufacturing method of the MBDL-NanoMat and characteristics of each layer. C) Application of the MBDL-NanoMat in postoperative treatment of breast cancer. D) Complete wound healing with multiple anticancer/antibacterial functions of the MBDL-NanoMat.

the healing process of bacteria-infected wounds that typically follow TNBC surgery.

To this end, electrospun nanofibrous matrices offer significant advantages in biomedical applications, including drug delivery, tissue engineering, and cancer therapy. Their large surface area and high drug-loading capacity are particularly beneficial in these contexts.^[6] When implanted using minimally invasive surgery, these scaffolds enable high local drug accumulation while minimizing systemic side effects.^[6] The main objectives of loco-regional cancer therapy are to prevent the recurrence of tumors and to facilitate post-operative wound healing. However, current strategies often cannot meet the diverse therapies (anticancer and/or antibacterial) and physicochemical/mechanical requirements, such as elasticity and adherence. While integrating multiple drugs into a nanofibrous matrix may offer synergistic anticancer and antibacterial effects, achieving sufficient multifunctional therapeutic performance and proper fitting to the post-surgical site remains a significant challenge.^[7] Many nanofiber (NF) matrices produced by electrospinning currently face challenges, such as uncontrolled drug release and loss of functionality upon disintegration, limiting their effectiveness in wound healing. However, these limitations can be addressed by employing a multifunctional bioactive dual-layered nanofibrous matrix (MBDL-NanoMat). Herein, we developed the MBDL-NanoMat composed of a hydrophilic (HyPhil) layer with gelatin and copper peroxide nanoparticles (Cu NPs), and a hydrophobic (HyPhob) layer made from poly(ϵ -caprolactone) (PCL), poly-citrate (POC), and rapamycin (RPM) fabricated via electrospinning (Figure 1B). Each layer can incorporate therapeutic agents with varying physicochemical properties, allowing programmed drug release profiles. Furthermore, the thickness of the MBDL-NanoMat can be custom-designed to suit the specific needs of both the patient and surgeon for enhanced adjuvant cancer therapy (Figure 1B).

This MBDL-NanoMat is designed for local application to suppress tumor recurrence, prevent post-operative infections, and promote recovery of the injured site (Figure 1C). A fast-disintegrating HyPhil layer, encapsulating therapeutic agents such as Cu NPs, was attached to the tumor-resected region (mucosa tissue), releasing therapeutic agents immediately (Figure 1C). Meanwhile, a slow-disintegrating HyPhob layer containing therapeutic molecules, such as RPM, can stretch to the wound's shape, facilitating easy suturing and providing sustained drug release following the TNBC removal surgery (Figure 1C). The HyPhob layer may protect the wound site from further infection and provide sufficient time for damaged tissue to recover. Complete wound healing is achieved through the multiple anticancer and antibacterial functions of the MBDL-NanoMat (Figure 1D). Cu NPs in the HyPhil layer generate hydroxyl radicals, enabling chemodynamic therapy (CDT) by the self-generation of H_2O_2 and a copper ion-mediated Fenton-like reaction in the tumor and/or bacterial microenvironment.^[8] This process promotes anticancer effects via ferroptosis and cuproptosis induction.^[9] Meanwhile, the sustained release of RPM from the HyPhob layer provides prolonged chemotherapy (CT) and antibacterial effects through mammalian target of rapamycin (mTOR) inhibition.^[10] In addition, the application of near-infrared (NIR) laser irradiation in photothermal therapy (PTT), serves to enhance the effectiveness of anticancer and an-

tibacterial actions, thus significantly contributing to the wound healing process. The integration of this MBDL-NanoMat with localized NIR light irradiation enables the employment of various therapeutic modalities, including CT, CDT, PTT, ferroptosis, and cuproptosis. The MBDL-NanoMat's ability to mediate both immediate and sustained drug release ensures pronounced anti-recurrence and antibacterial efficacy.

In brief, this study offers novel and valuable insights into the development of a combinational therapeutic approach that incorporates multiple anticancer mechanisms within multi-functional bioactive dual-layered nanofibrous matrices. This innovative design not only enhances the efficacy of TNBC therapy but also facilitates improved post-surgical wound healing. Furthermore, this strategy addresses the dual challenges of tumor recurrence and bacterial infections after surgery, providing a comprehensive solution for both cancer treatment and wound management.

2. Results and Discussion

2.1. Characterization of the MBDL-NanoMat

Cu NPs were synthesized with a slight modification.^[8a] The particle properties of the Cu NPs were investigated (Figure S1, Supporting Information). The spherical shapes were observed by transmission electron microscopy (TEM), and their diameters (10.4 ± 2.1 nm) were directly acquired from the images. Unimodal particle size distribution was observed, and the zeta potential value of Cu NPs was -4.24 ± 2.24 mV. Moreover, copper-based nanomaterials exhibit a strong and adjustable localized surface plasmon resonance within the NIR biological window, enabling high light-to-heat conversion efficiency for PTT.^[11] The Cu NPs exhibited a temperature increase of 16.3 ± 0.4 °C for 3 min under NIR laser irradiation (808 nm, 0.5 W cm^{-2}) (Figure S1C, Supporting Information).

The proton nuclear magnetic resonance (1H NMR) spectrum of POC displayed characteristic methylene peaks ($-CH_2-$ at 1.269, 1.529, and 3.973 ppm in peaks a, b, and c), corresponding to 1,8-octanediol (Figure S2, Supporting Information). The peaks in the range of 2.670–2.838 ppm ($-CH_2-$ in peak d) were attributed to citric acid.^[12a] The molecular weight (MW) of POC, determined by gel permeation chromatography (GPC), was 32.3 kDa. To optimize the composition of the MBDL-NanoMat structure for future biomedical applications, various concentrations of PCL (3%, 5%, 7%, and 10% (w/v)) and gelatin (0%, 3%, 5%, and 7% (w/v)) were blended in different ratios to achieve a total concentration of 10% (w/v). The composition was selected based on the mechanical properties (i.e., tensile strength and elongation; Figure S3, Supporting Information). As the proportion of PCL decreased, the tensile strength also decreased. Similarly, the elongation value was significantly reduced with the inclusion of gelatin. To enhance the tensile strength, POC (0.2, 0.5, and 1% (w/v)) was added due to its elastomeric properties, which have been used in tissue regeneration, bioimaging, and gene delivery.^[6c,12] Tensile strength increased with the addition of POC but declined sharply at 1%. In contrast, elongation increased up to 0.2% POC but significantly decreased beyond that point (Figure S3, Supporting Information). Based on these findings, the compositions of the HyPhob layer (PCL: POC = 7:0.2% (w/v)) and the HyPhil layer (3% (w/v) gelatin) were selected for

further modification. The PCL/POC/RPM (PPR) nanofibrous matrix (HyPhob) was prepared by blending 0.5% (w/v) RPM into the PCL-POC mixture, while the gelatin/Cu NPs (GC) nanofibrous matrix (HyPhil) was prepared by incorporating 0.5% (w/v) Cu NPs into the gelatin dispersion. The MBDL-NanoMat was created using a layering method, with the first electrospinning process of the HyPhil layer, followed by the deposition of the HyPhob layer onto the HyPhil layer (Figure 2A). Heat (40 °C) was applied to dry and harden the PCL/POC layer, while the gelatin layer melted, facilitating adhesion between the two layers.^[13] The thickness of the MBDL-NanoMat increased in a time-dependent manner with the electrospinning time (Figure S4A, Supporting Information). To determine the optimal thickness for this experiment, the wound was sutured using NF mats of varying thickness. NF mats were fabricated through electrospinning for 1, 2, and 4 h, and their properties were analyzed accordingly. The NF mat produced with 1 h of electrospinning was too thin and quickly dissipated from the wound, while the other formulations remained intact (Figure S4B, Supporting Information). The NF mat fabricated with 4 h of electrospinning failed to achieve sufficient temperature elevation for the PTT effect upon NIR laser irradiation. The NF mat produced by 2 h of electrospinning demonstrated adequate temperature increase compared to the others ($p < 0.05$) (Figure S4C, Supporting Information). Modulating the thickness of the NF mat is one of the advantages of our fabrication method. During surgery in clinics, the surgeon can adjust the thickness as desired, allowing customization based on the patient's specific wound condition.

The hydrophilic and hydrophobic properties of the nanofibrous matrix were evaluated by water contact angle (WCA) (Figure 2B). It has been demonstrated that a WCA in the range of 40–80° exhibits the greatest adhesion on the skin surface.^[6c,14] In our platform, the WCA of the HyPhil layer was $59.8^\circ \pm 3.4^\circ$, which significantly decreased over time, indicating the hydrophilic property. On the contrary, the HyPhob matrix exhibited $133.9^\circ \pm 5.9^\circ$, indicating hydrophobicity,^[15] and incubation time-dependent reduction of WCA was observed.

The texture and sectional morphology of the MBDL-NanoMat group were explored by a field emission-scanning electron microscope (FE-SEM; Figure 2C; Figure S5, Table S1, Supporting Information). The NF was positioned with the HyPhil layer (stained pink with rhodamine B (Rho B)) facing upward for FE-SEM imaging, and distinct structural differences were confirmed between the HyPhil and HyPhob layers. Both layers exhibited homogeneous and bead-free NF networks in FE-SEM images. Notably, the distribution of Cu NPs in the HyPhil layer was observed in the SEM-energy-dispersive X-ray spectroscopy (EDS) mapping image, and the atomic content of Cu was 4% (Figure S5, Supporting Information). The entrapment efficiency (EE) of RPM in the HyPhob layer was $89.5 \pm 0.8\%$, and the mean diameter of NF was 298.8 ± 52.1 nm in Table S1 (Supporting Information). In the HyPhil layer, the EE of Cu NPs was $26.4 \pm 2\%$, and its mean diameter was 418.9 ± 42.2 nm in Table S1 (Supporting Information).

The crystalline-to-amorphous transformation of drug cargos in each layer was analyzed using X-ray diffraction (XRD) (Figure S6, Supporting Information). As shown in the amorphous structure, XRD patterns of the HyPhil and HyPhob groups displayed no obvious diffraction peaks. Notably, the electrospinning process

appears to significantly reduce the crystallinity of the molecular structure of RPM within the HyPhob layer.

Despite the division of the MBDL-NanoMat into distinct HyPhil and HyPhob layers, the porous structure of each layer allows it to function as a semipermeable membrane, resembling the natural skin. This characteristic facilitates the transport of oxygen and moisture, modulating cellular activity.^[16] Excessive moisture loss dries the skin, hindering wound healing and making the reduction of transdermal water crucial for efficient recovery.^[17] Healthy skin typically exhibits water vapor permeability (WVP) of $204 \text{ g m}^{-2} \text{ day}^{-1}$, but this rate increases when the skin is damaged.^[16b,18] The WVP values for HyPhil, HyPhob, and MBDL-NanoMat groups indicated 5675.9 ± 233.9 , 5024.8 ± 241.5 , and $5420.8 \pm 100.2 \text{ g m}^{-2} \text{ day}^{-1}$, respectively, which were lower than that of the gauze control ($6208.8 \pm 455.5 \text{ g m}^{-2} \text{ day}^{-1}$) (Figure S7, Supporting Information). Comparable values are shown between the gauze and MBDL-NanoMat groups. Considering that gauze is a commercially available wound management dressing, the developed nanofibrous matrices can provide adequate moisture conditions for wound healing. Additionally, the wetting properties may be attributed to the absorption of exudate from the wound into the MBDL-NanoMat.

The Fourier transform infrared (FT-IR) data revealed the chemical structures of the HyPhil (gelatin/Cu NPs) and HyPhob (PCL/POC/RPM) nanofibrous matrices (Figure 2D; Figure S8, Supporting Information). To confirm the chemical structure of the HyPhil layer, FT-IR plots of Cu NPs and pristine gelatin NF were acquired (Figure S8A, Table S2, Supporting Information). Since Cu NPs were synthesized with the addition of polyvinylpyrrolidone (PVP), the FT-IR of Cu NPs primarily contained the characteristic peaks of PVP.^[8a] However, the small peak at 457 cm^{-1} can be attributed to Cu–O stretching, indicating the complexation of Cu(II) with PVP during the formation of Cu NPs (Figure S8, Supporting Information). Most peaks were identical between the gelatin and gelatin/Cu NPs groups, confirming the absence of any significant covalent and/or coordinated bonding of Cu NPs with gelatin. However, in the FT-IR spectrum of the HyPhil layer (Figure 2D), the newly observed peak at 424 cm^{-1} , attributed to Cu–O stretching, ensured the incorporation of Cu NPs in the HyPhil part of the nanofibrous membrane. The prominent PCL-specific peaks indicated the existence of PCL in this layer (Figure 2D; Figure S8, Supporting Information). Additionally, the presence of POC in the HyPhob can be substantiated by the exclusive appearance of O–H and C–O out-of-plane deformation at $639/614$ and 421 cm^{-1} , respectively (Figure S8B, Table S3, Supporting Information). The inclusion of RPM in HyPhob was confirmed by the newly observed peaks at 1460 and 1325 cm^{-1} , attributed to N–H bending and amide-III (C–N stretching) of the secondary amide group of RPM.

The tensile strength of the HyPhob and MBDL-NanoMat NF groups was 12 ± 0.7 and $15.6 \pm 1.5 \text{ MPa}$, respectively ($p < 0.05$) (Figure 2E). Given that the elasticity of human skin is ≈ 2 – 16 MPa ,^[6c,19] the elasticity of the developed NF was considered adequate as a skin replacement. In contrast, the HyPhil layer exhibited negligible tensile strength. The elongation values of HyPhil, HyPhob, and MBDL-NanoMat groups were 15, 301.7, and 307.3%, respectively (Figure 2E). The HyPhob layer seems to con-

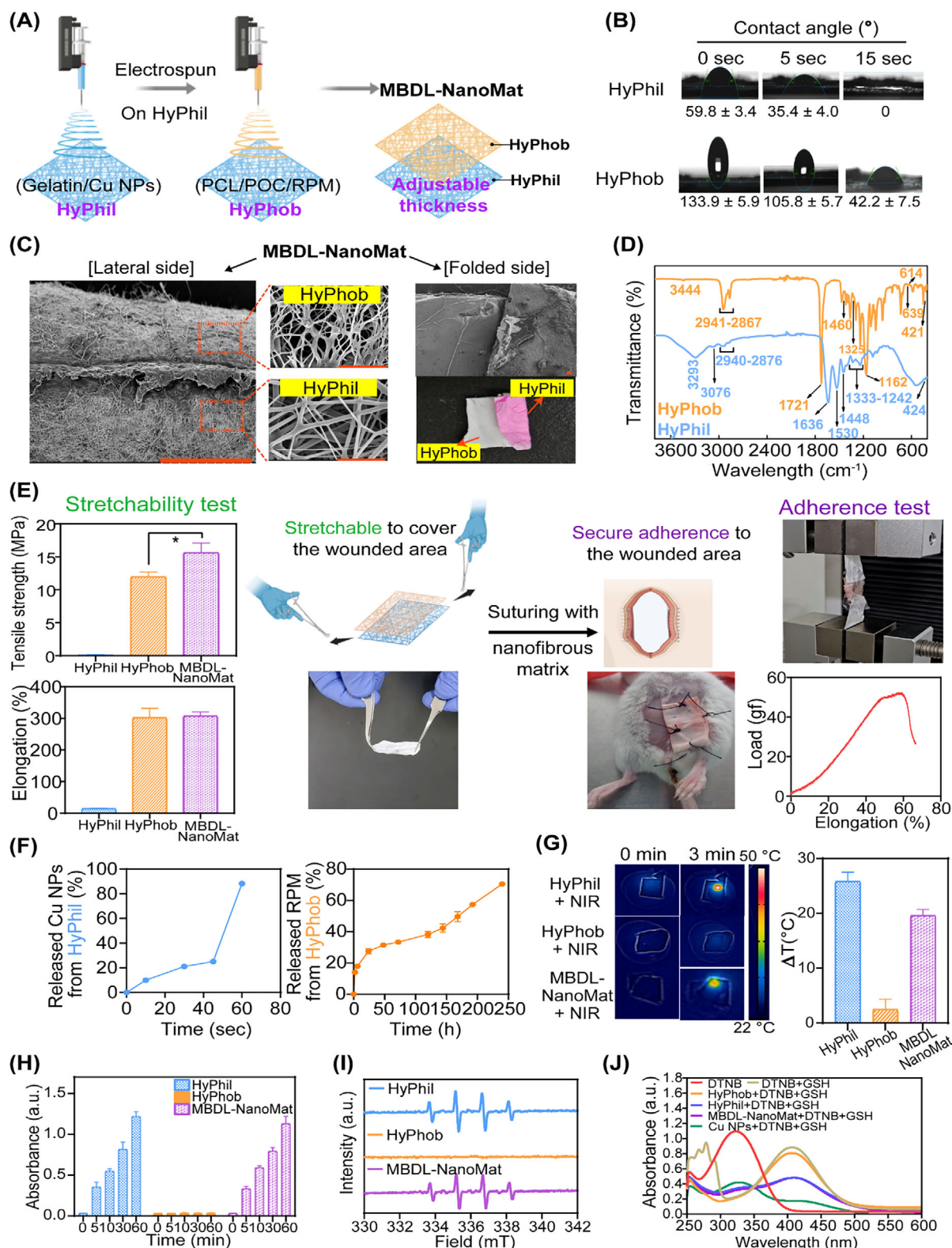


Figure 2. Physicochemical properties of MBDL-NanoMat. A) Schematic illustration for the fabrication of MBDL-NanoMat. B) WCA data of the HyPhil and HyPhob layers at predetermined times (0, 5, and 15 s). Each value represents mean ± SD ($n = 3$). C) FE-SEM images of HyPhil and HyPhob layers as components of the MBDL-NanoMat. The lateral side (scale bar for original image: 100 μm, scale bar for magnified image: 5 μm) and folded side (scale bar: 100 μm) are shown. D) FT-IR data of the HyPhil and HyPhob groups. E) Schematic diagram of the stretchable, suturable, and adhesive properties of MBDL-NanoMat. Stretchability test (tensile strength and elongation measurement) data of HyPhil, HyPhob, and MBDL-NanoMat groups

tribute significantly to the elongation properties of the MBDL-NanoMat group.

In vitro adhesion test of the nanofibrous matrix was conducted using the universal material machine (Figure 2E). Misalignment traction tests were performed when the skin and MBDL-NanoMat were securely bonded. The results demonstrated that the designed nanofibrous matrix could withstand a tensile force of ≈ 0.5 N without breaking and exhibited an elongation of $\approx 60\%$ relative to its original length (Figure 2E). Additionally, the adhesion strength between the skin and MBDL-NanoMat was sufficient to support a weight of 50 g (Figure S9, Supporting Information).

The interactions between MBDL-NanoMat and the skin layer were elucidated by FT-IR analysis (Figure S10, Supporting Information). In the hydrophilic portion of the membrane, the distinct sharp peak at 1722 cm^{-1} , indicating the presence of $>\text{C}=\text{O}$ stretching of $-\text{COOH}$ from gelatin, was not observed in the MBDL-NanoMat + skin specimen. Similarly, the low-intensity peak at 1737 cm^{-1} , attributable to the $>\text{C}=\text{O}$ stretching of $-\text{COOH}$ in the skin group, shifted significantly to 1750 cm^{-1} in the MBDL-NanoMat + skin specimen. The broad $>\text{C}=\text{O}$ stretching peaks of $-\text{CONH}_2$ (Amide-I) at 1647 and 1640 cm^{-1} in MBDL-NanoMat and skin, respectively, became very sharp and shifted to 1627 cm^{-1} in the MBDL-NanoMat + skin group. This observation demonstrated the involvement of $>\text{C}=\text{O}$ of $-\text{CONH}_2$ of skin in coordination with a hydrophilic portion of MBDL-NanoMat. Significant modification in the hydrogen-bonding environment was observed along with the shifting of $>\text{C}=\text{O}$ stretching of $-\text{COOH}$ and $-\text{CONH}_2$ from 1737 and 1640 cm^{-1} in the skin group to 1758 and 1649 cm^{-1} in the Cu NPs + skin group, respectively. Therefore, it can be concluded that MBDL-NanoMat exhibited adhesion properties with skin through hydrogen bonding (involving various hydrophilic functionalities of HyPhil and skin) and chemical bonding (involving Cu (II) of HyPhil and skin).

The attachment mechanism between the HyPhil and HyPhob layers forming the MBDL-NanoMat, as well as the adhesive interactions between the MBDL-NanoMat and skin, were further evaluated using X-ray photoelectron spectroscopy (XPS) analyses (Figures S11, S12, Table S4, Supporting Information). In the wide scan survey plots (Figure S11, Supporting Information), the HyPhil layer contains signals of Cu 2p and N 1s orbitals, confirming the presence of Cu NPs and gelatin. On the other hand, the N 1s signal of HyPhob was weak, but the distinct N 1s peak at 400.48 eV in the narrow scan spectrum of HyPhob inferred the presence of nitrogen from RPM in HyPhob. In the HyPhob group, the distinct C 1s peaks at 284.34 , 285.07 , 285.66 , 286.72 , 288.93 , and $290.09/291.65\text{ eV}$ could be attributed to $>\text{C}=\text{C}<$, $\text{C}-\text{C}$, $-\text{C}-\text{O}-\text{C}-$, $-\text{C}-\text{OH}$, $>\text{C}=\text{O}$, and satellite peaks, respectively.^[20] Of these, the peak at 285.66 eV , which was

absent in the HyPhil layer, indicated the presence of RPM in the HyPhob layer. Importantly, this peak was also present in the C 1s spectra of MBDL-NanoMat and MBDL-NanoMat/skin groups at 285.91 and 285.71 eV , respectively, indicating the inclusion of RPM in the HyPhob layer. In the HyPhil group, the presence of $-\text{NH}_3^+$ of gelatin (i.e., zwitterionic forms) could be inferred from the N 1s peak at 402.79 eV . The significant shifting of O 1s peaks of $-\text{COOH}/-\text{CONH}_2$ and $-\text{C}-\text{O}-\text{C}$ from 532.61 and 534.87 eV in HyPhob to $530.55/531.82/532.56$ and 534.66 eV in MBDL-NanoMat and $530.09/531.43/532.97$ and 535.51 eV in MBDL-NanoMat/skin, respectively, inferred the formation of coordinate and/or covalent interactions of Cu (II). In fact, the presence of Cu 2p signals in the wide scan survey plot of the MBDL-NanoMat group also suggested the presence of the HyPhil portion, which is involved in binding with skin to generate MBDL-NanoMat/skin. In the HyPhil group, the deconvoluted Cu 2p spectrum contains three distinct peaks at 929.58 , 936.73 , and 952.07 eV corresponding to Cu $2p_{3/2}$, the satellite peak of Cu $2p_{3/2}$, and Cu $2p_{1/2}$ of Cu (II), respectively. These peaks shifted to 931.20 , 940.28 , and 949.38 eV , respectively, in the MBDL-NanoMat group, supporting the co-existence of covalent and coordinated bonding. However, in the MBDL-NanoMat/skin group, the prominent peaks at 927.53 and 943.85 eV inferred the presence of Cu(I). The emergence of the new Cu(I) moiety indicated the in situ reduction of Cu (II) in the HyPhil layer during its adhesion with skin. The shifting of Cu (II) peaks in the MBDL-NanoMat/skin group compared to the MBDL-NanoMat group indicated the co-existence of covalent and coordinated bonding. Overall, the formation of the MBDL-NanoMat from the HyPhob and HyPhil layers, as well as the adhesion between the MBDL-NanoMat and skin, can be attributed to the formation of mixed chemical linkages, including coordinate and covalent bonds involving Cu (II) and/or Cu (I).

The HyPhil, HyPhob, and MBDL-NanoMat specimens were placed on a buffer-soaked filter paper to investigate their wetting properties (Figure S13, Supporting Information). The HyPhil membrane was completely wetted within 30 s (Figure S13A, Supporting Information). This fast-wetting phenomenon could be attributed to the hydrophilicity of gelatin and the physicochemical characteristics (e.g., nano-size mesh) of the nanofibrous matrix. Given that the hydrophilic part of the MBDL-NanoMat contacts the wound surface and absorbs exudate, its rapid wetting characteristics may enhance absorption. Moreover, the exudate absorption by the MBDL-NanoMat may prevent water loss by evaporation, thereby promoting wound healing. In contrast, the HyPhob and MBDL-NanoMat groups did not exhibit wetting properties until 96 h due to their hydrophobic nature (Figure S13B, Supporting Information).

Additionally, the disintegration behavior was evaluated by measuring the weight of the freeze-dried product (Figure S14, Supporting Information). It showed that the HyPhil layer was

are shown. Each value represents mean \pm SD ($n = 3$). * $p < 0.05$, between indicated groups. One-way ANOVA with Tukey's *post hoc* test. The adhesive performance of the designed nanofibrous matrix (as an elongation-load plot) is presented. F) Release profiles of Cu NPs from the HyPhil layer and RPM from the HyPhob layer. Each value represents mean \pm SD ($n = 3$). G) Infrared thermal images of HyPhil + NIR, HyPhob + NIR, and MBDL-NanoMat + NIR groups. Temperature change data are plotted. Each value represents mean \pm SD ($n = 3$). H) TMB assay for assessing hydroxyl radical generation of HyPhil, HyPhob, and MBDL-NanoMat groups. Each value represents mean \pm SD ($n = 4$). I) ESR data of HyPhil, HyPhob, and MBDL-NanoMat groups. J) Extracellular GSH assay. Absorbance profiles of DTNB, DTNB + GSH, HyPhob + DTNB + GSH, HyPhil + DTNB + GSH, MBDL-NanoMat + DTNB + GSH, and Cu NPs + DTNB + GSH groups are plotted. Average values are plotted ($n = 3$).

completely disintegrated within 1 min, while the HyPhob and MBDL-NanoMat samples did not exhibit complete disintegration properties until 96 h (Figure S14A, Supporting Information). The relative weight values, expressed as the ratios of the remaining amount to the initial weight, of the HyPhil, HyPhob, and MBDL-NanoMat groups were $9.9 \pm 4.8\%$, $67.5 \pm 11.8\%$, and $47.5 \pm 12\%$, respectively, at each final time point (Figure S14B, Supporting Information). The lower relative weight ratio of the MBDL-NanoMat group compared to the HyPhob group is likely due to the complete disintegration of the HyPhil layer. These findings indicate that the HyPhil matrix from the MBDL-NanoMat can be disintegrated immediately, while the HyPhob matrix in the MBDL-NanoMat may display a low disintegration rate.

The release kinetic properties of Cu NPs from the HyPhil layer and RPM from the HyPhob layer were explored in phosphate-buffered saline (PBS, pH 6.5), mimicking the tumor microenvironment (Figure 2F).^[21] The release of Cu NPs from the HyPhil was measured at 10, 30, 45, and 60 s, reaching $88.2 \pm 0.2\%$ within 60 s. The HyPhil layer is composed of gelatin, with a melting point of 35–38 °C. It is expected that the HyPhil membrane may be melted at 37 °C (as the temperature of the release test), and it will be disintegrated, accelerating the release of Cu NPs as shown in Figures S13A,S14 (Supporting Information). It can be inferred that at the release test temperature (37 °C), the membrane melts and disintegrates, accelerating the release of drug cargo (Figures S13A,S14, Supporting Information). In contrast, the released RPM from the HyPhob was measured at 2, 6, 24, 48, 72, 120, 144, 168, 192, and 240 h. The HyPhob layer showed a sustained release profile of RPM ($70.5 \pm 1.5\%$ over 240 h). As predicted from the results of wetting and disintegration studies (Figures S13,S14, Supporting Information), the MBDL-NanoMat can rapidly release Cu NPs in the early phase, which is beneficial for achieving prompt reactive oxygen species (ROS)-assisted anticancer and antibacterial effects. Subsequently, the sustained release of RPM and accumulated Cu NPs ensured prolonged anticancer and wound healing effects.

To investigate the photothermal behavior of the MBDL-NanoMat, temperature changes were monitored during NIR laser irradiation for 3 min (Figure 2G). Notably, the temperature change (ΔT) values of the HyPhil and MBDL-NanoMat groups were 25.9 ± 1.7 and 19.7 ± 1.1 °C, respectively. Although the temperature change in MBDL-NanoMat is lower than that of the HyPhil layer, the increase is sufficient to induce a hyperthermia state considering normal body temperature in the case of in vivo application. Conversely, a minimal temperature increase was observed in the HyPhob group under the same condition. Thus, the Cu NP-incorporated HyPhil layer appears to function as a photothermal agent in this study, making it a promising candidate for local cancer therapy, particularly in treating bacterial infections.

The potential for hydroxyl radical generation from the nanofibrous matrix was assessed using 3,3',5,5'-tetramethylbenzidine (TMB) and TiOSO_4 assays (Figure 2H; Figure S15, Supporting Information). TMB can be oxidized by OH radicals, resulting in a blue-green complex with maximum absorbance at 650 nm. Cu NPs can simultaneously release Cu^{2+} and H_2O_2 , making them a promising agent for cascade self-hydroxyl radical production.^[8a] Although the H_2O_2 generation rate in cancer cells is fast, its in-

trinsic concentration is known to be insufficient for the effective destruction of cancer by CDT.^[22] Therefore, the self-generation of H_2O_2 and copper ions released from Cu NPs may boost the efficiency of OH radical generation for CDT and antibacterial applications. As shown in Figure S15 (Supporting Information), the OH radical generation capability of Cu NPs at acidic pH (pH 5.5) indicates the tumor microenvironment was higher than normal physiological pH (pH 7.4). The self-generation efficacy of H_2O_2 by Cu NPs was evaluated using a TiOSO_4 -based assay, corresponding to $\approx 2.8 \mu\text{M}$ of H_2O_2 under the given experimental conditions. HyPhil and MBDL-NanoMat groups (with Cu NPs) exhibited a time-dependent increase in absorbance at 650 nm, while the HyPhob group (without Cu NPs) did not show such a pattern (Figure 2H). These findings support the enhanced self-production of H_2O_2 from Cu NPs and its conversion to OH radical based on the copper ion-mediated Fenton-like reaction. Additionally, we investigated the impact of GSH addition and NIR light irradiation on the generation of hydroxyl radicals (Figure S16, Supporting Information). The results showed that the introduction of GSH led to an increased production of hydroxyl radicals compared to the group without GSH (Figure 2H; Figure S16, Supporting Information). GSH can reduce Cu^{2+} to Cu^+ and Cu^+ can produce hydroxyl radicals by reacting with H_2O_2 , leading to the enhanced chemodynamic effect (Figure 1). On the contrary, NIR laser irradiation did not significantly elevate the radical generation (Figure 2H; Figure S16, Supporting Information).

Electron spin resonance (ESR) spectra were acquired to identify the generation of OH radicals, using 5,5-dimethyl-1-pyrroline N-oxide (DMPO) as a spin-trapping agent (Figure 2I; Figure S17, Supporting Information). Cu NPs produce H_2O_2 spontaneously in the presence of H_2O and copper ions (from Cu NPs), facilitating the catalysis of H_2O_2 into OH radicals for enabling the CDT effect.^[8a,23] As shown in Figure 2I, a 1:2:2:1 peak pattern of OH radical was clearly detected in the HyPhil and MBDL-NanoMat groups. No characteristic peak pattern was observed in the HyPhob group. Therefore, the observed data may imply the successful generation of OH radicals in the designed double-sided nanofibrous matrix. Additionally, after NIR laser irradiation (808 nm, 0.5 W cm^{-2}) for 3 min, a 1:2:2:1 peak pattern of OH radical was observed in the HyPhil + NIR light and MBDL-NanoMat + NIR light groups. In contrast, it was not observed in the HyPhob + NIR light group (Figure S17, Supporting Information). It seems that the presence of NIR light irradiation does not significantly influence the OH radical generation efficiency.

The extracellular glutathione (GSH) depletion ability of the nanofibrous matrix was investigated (Figure 2J).^[24] The level of GSH decreased by a catalytic reaction between Cu^{2+} and GSH to generate Cu^+ and glutathione disulfide (GSSG). Cu^{2+} facilitates the oxidation of GSH to GSSG, thereby inhibiting the conversion of 5,5'-dithiobis (2-nitrobenzoic acid) (DTNB) to TNB. The HyPhob + DTNB + GSH group displayed a slightly lower absorbance profile than the DTNB + GSH group, implying a negligible GSH depletion effect of the HyPhob layer. The absorbance profiles of HyPhil + DTNB + GSH and MBDL-NanoMat + DTNB + GSH groups were intermediate between those of DTNB + GSH and Cu NPs + DTNB + GSH groups. Although incorporating Cu NPs into the NF mat influenced the DTNB-TNB conversion efficiency, the MBDL-NanoMat group still displayed GSH depletion capability.

2.2. In Vitro Anticancer Activities

The anticancer capacity of the nanofibrous matrix was evaluated by antiproliferation, intracellular ROS, apoptosis, cellular GSH, lipid peroxidation (LPO), malondialdehyde (MDA), and western blot assays (Figure 3). An experimental system was designed based on the different drug release patterns of the double-sided nanofibrous matrix (i.e., immediate release of Cu NPs from the HyPhil versus sustained release of RPM from the HyPhob) (Figure 3A). Given that most Cu NPs were released from the HyPhil layer during the initial period (i.e., within 60 s), the media collected at these early time points were subsequently added to the cells. As RPM was released from the HyPhob layer in a sustained manner, media obtained from the late time points (i.e., 24–144 h) were used to evaluate toxicity. The control group showed negligible toxicity over the tested period. In contrast, HyPhil, HyPhil + NIR, MBDL-NanoMat, and MBDL-NanoMat + NIR groups exhibited time-dependent antiproliferation capability (Figure 3B). The NIR laser irradiation group resulted in elevated antiproliferation efficiency compared to the HyPhil and MBDL-NanoMat groups (without NIR laser irradiation) ($p < 0.05$). NIR light-assisted PTT seems to contribute to increased antiproliferation activity in 4T1 cells. Moreover, sustained release of RPM (for mTOR protein kinase inhibition) from the HyPhob and MBDL-NanoMat groups exhibited cytotoxic potential. Photothermal conversion further enhanced the antiproliferation efficacy of the MBDL-NanoMat group compared to the non-irradiated group ($p < 0.05$). This implies that a combination of CDT, PTT, ferroptosis, and cuproptosis from the HyPhil layer has more significant antiproliferative potential than a single therapeutic option. Additionally, the sustained release of RPM is expected to provide long-term anticancer effects. To highlight the platform's intrinsic multi-modal therapeutic potential, we focused on comparing treatment groups employing different therapeutic modalities. While some commercial chemotherapeutics could indeed provide a benchmark, the exact anticancer mechanisms were different from our formulations. We believe our current data sufficiently demonstrate the strong anti-proliferative effect of MBDL-NanoMat through endogenous copper-based mechanisms and synergistic therapies with RPM.

Intracellular ROS levels following the application of HyPhob, HyPhil, HyPhil + NIR, MBDL-NanoMat, and MBDL-NanoMat + NIR groups were measured in 4T1 cells (Figure 3C). The fluorescence intensity values (indicating ROS level) of the HyPhob, HyPhil, HyPhil + NIR, MBDL-NanoMat, and MBDL-NanoMat + NIR groups were higher than the control group. Notably, the HyPhil + NIR group had a higher ROS level than the HyPhil group. Photothermal conversion in cancer cells seems to contribute to increased cellular ROS levels. The MBDL-NanoMat + NIR group exhibited the highest cellular ROS levels among all tested groups ($p < 0.05$). The multi-therapeutic approaches may provide combination effects in terms of cellular ROS generation.

The population percentages of apoptotic cells were assessed following the application of HyPhob, HyPhil, HyPhil + NIR, MBDL-NanoMat, and MBDL-NanoMat + NIR groups on 4T1 cells (Figure 3D). The lower right (LR) and upper right (UR) panels represent the early and late apoptotic phases, respectively. Therefore, the combined population of LR and UR panels may be utilized to demonstrate our system's ability to induce apoptosis

efficiently. The degree of induced apoptosis for all tested groups was higher than observed in the control group. NIR light irradiation to HyPhil-treated cells significantly increased the apoptosis population based on CDT and PTT. Interestingly, a significantly higher percentage in the LR + UR quadrant was observed in the MBDL-NanoMat + NIR group compared to the other groups ($p < 0.05$), showing greater apoptosis induction efficiency. This result is attributed to the combined therapeutic effects of CT, CDT, and PTT.

The GSH depletion ability of Cu NPs released from the nanofibrous matrix was measured using a colorimetric assay (Figure 3E). The relative GSH depletion ratios (compared to the control group) of the HyPhil, HyPhil + NIR, MBDL-NanoMat, and MBDL-NanoMat + NIR groups were found to be 40%, 33%, 32.7%, and 33.2%, respectively. This finding indicated that Cu^{2+} is reduced to Cu^+ with the conversion of GSH to GSSG. This GSH depletion can elevate ROS levels in cancer cells, ultimately enhancing the efficacy of CDT.^[23] These data suggest that the incorporated Cu NPs in the nanofibrous matrix system may effectively contribute to GSH depletion in cancer cells.

Lipid ROS levels following the application of nanofibrous matrix were evaluated to determine the degree of ferroptosis induction in 4T1 cells (Figure 3F). The fluorescence intensity (indicating lipid ROS level) of the HyPhob group was 4.6-fold higher than that in the control ($p < 0.05$). The accumulated intracellular RPM (following sustained release from the HyPhob layer) seems to act as a ferroptosis sensitizer in cancer cells.^[25] The lipid ROS level of the HyPhil group was higher than the control group. Cu NPs (following immediate release from the HyPhil layer) may convert membrane lipids to lipid ROS, and this LPO may lead to the induction of ferroptosis in cancer cells.^[9a,26] Moreover, NIR laser application with the HyPhil group contributed to a 1.3-fold increase in LPO level compared to the HyPhil group, suggesting that photothermal conversion contributes to the increase in LPO. Notably, the MBDL-NanoMat + NIR group displayed a higher degree of LPO compared to the other groups ($p < 0.05$), highlighting the combination effect of RPM (from the HyPhob), ROS (from the HyPhil), and photothermal effect.

MDA is one of the products of LPO; thus, cellular MDA levels were measured (Figure 3F). The HyPhob group displayed increased fluorescence intensity compared to the control, which may be attributed to the ferroptosis-sensitizing effect of RPM. This interpretation is supported by the results of the lipid ROS assay. Elevated MDA levels were observed in the HyPhil group compared to the control group, which can be attributed to the presence of copper ions. Notably, the MBDL-NanoMat + NIR group displayed significantly higher MDA levels than all other experimental groups ($p < 0.05$). The results of both the LPO and MDA assays indicate that the HyPhob, HyPhil, and NIR laser components contribute to ferroptosis induction in 4T1 cells.

Cuproptosis induction can be demonstrated by dihydrolipoamide S-acetyltransferase (DLAT) oligomerization and the destabilization of ferredoxin-1 (FDX1) and lipoyl synthase (LIAS) in cancer cells.^[9b,c] As revealed in Figure 3G and Figure S18 (Supporting Information), HyPhil, HyPhil + NIR, MBDL-NanoMat, and MBDL-NanoMat + NIR groups (containing Cu NPs) exhibited downregulation of DLAT, FDX1, and LIAS ($p < 0.05$), indicating the successful induction of cuproptosis. The GSH depletion potential of Cu NPs was also examined by

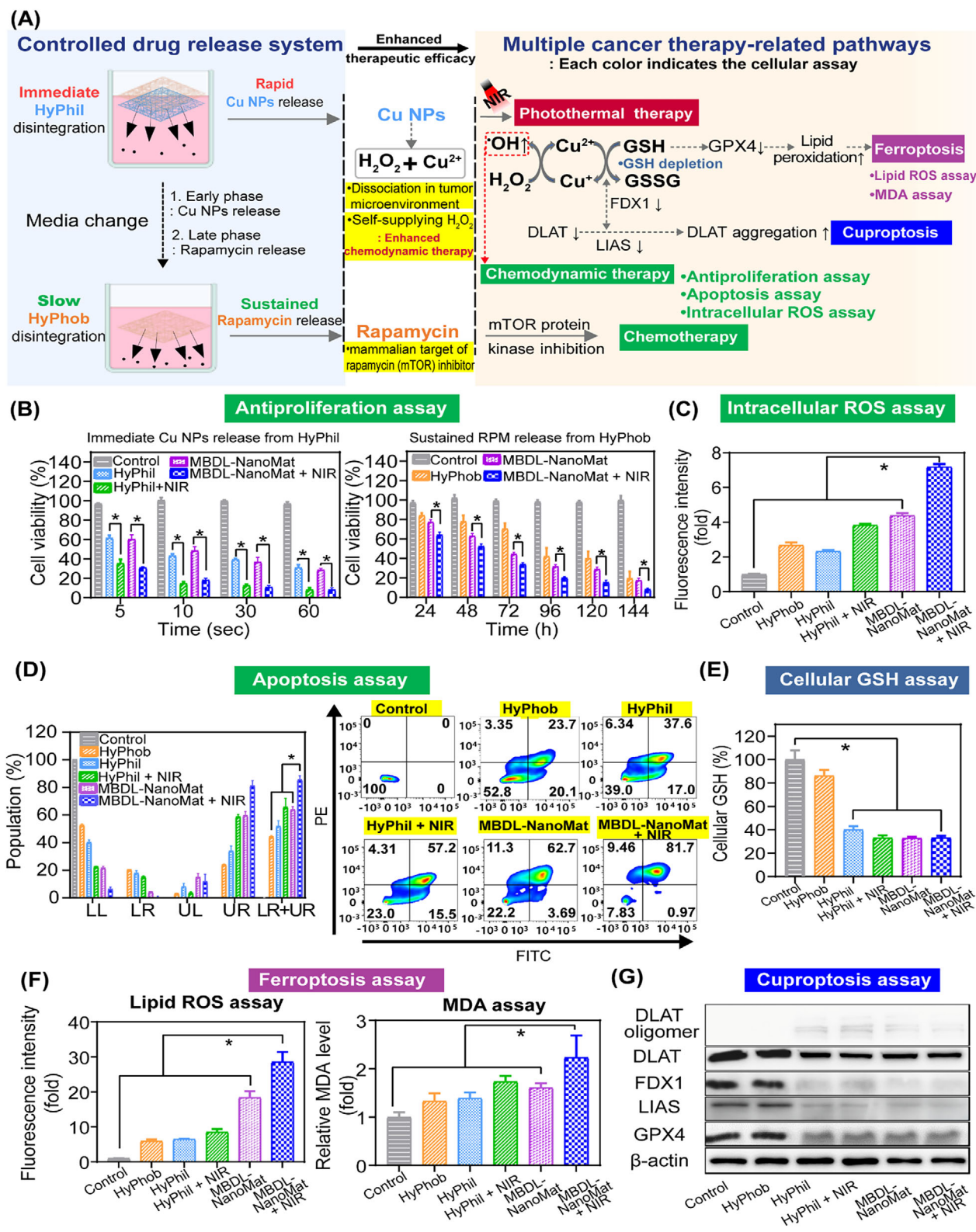


Figure 3. In vitro anticancer and antibacterial efficacies. A) Schematic illustration of cellular experimental system design for evaluating MBDL-NanoMat and multiple anticancer mechanisms. B) Antiproliferation efficacy test in 4T1 cells. Each point represents mean \pm SD ($n = 4$). * $p < 0.05$, between indicated groups. One-way ANOVA with Tukey's *post hoc* test. C) Intracellular ROS assay in 4T1 cells. Relative fluorescence intensity data of the control, HyPhob, HyPhil, HyPhil + NIR, MBDL-NanoMat, and MBDL-NanoMat + NIR groups are displayed. Data are shown as mean \pm SD ($n = 3$). * $p < 0.05$, between indicated groups. One-way ANOVA with Tukey's *post hoc* test. D) Apoptosis assay in 4T1 cells. Population (%) values of lower left (LL), lower right (LR),

glutathione peroxidase 4 (GPX4) level (Figure 3G; Figure S18, Supporting Information). The Cu^{2+} ions may convert GSH into GSSG, leading to the downregulation of GPX4. Relative GPX4 levels in HyPhil, HyPhil + NIR, MBDL-NanoMat, and MBDL-NanoMat + NIR groups (including Cu NPs) were lower than the control group ($p < 0.05$) (Figure S18, Supporting Information). These findings indicate GSH-GPX4 axis downregulation by Cu NPs released from the double-sided NF mat.

2.3. In Vitro Antibacterial Efficacy

The in vitro antibacterial efficacy of the HyPhob, HyPhil, HyPhil + NIR, MBDL-NanoMat, and MBDL-NanoMat + NIR groups was evaluated (Figure S19, Supporting Information). The mean colony-forming unit (CFU) amounts of the HyPhob, HyPhil, HyPhil + NIR, MBDL-NanoMat, and MBDL-NanoMat + NIR groups were lower than that of the control group. Notably, the MBDL-NanoMat + NIR group exhibited a lower CFU amount rather than the control, HyPhob, HyPhil, and HyPhil + NIR groups ($p < 0.05$). Cu NPs from the HyPhil layer and RPM from the HyPhob layer had bacteria-killing effects. The generation of OH radicals and photothermal conversion (upon NIR laser exposure) of Cu NPs, combined with the antibiotic function of RPM, resulted in bacterial killing. Additionally, as shown in Figure S19B (Supporting Information), the turbidity test data revealed dose-dependent antibacterial effects of Cu NPs and RPM.

2.4. Anticancer Potential in a 3D Tumor Spheroid Model

The 3D spheroid model is a valuable tool for simulating the breast cancer microenvironment, faithfully recapitulating its structural complexity and heterogeneity. Consequently, this model offers a more physiologically relevant platform for evaluating anticancer efficacy, better representing differentiated cellular functions, and providing more accurate predictions of in vivo responses to drug treatments. The developed MBDL-NanoMat system demonstrated significant growth inhibition in a 3D-cultured 4T1 tumor spheroid model, highlighting its potential for in vivo efficacy (Figure S20, Supporting Information). On day 4, the spheroid volumes of the control, HyPhob, HyPhil, HyPhil + NIR, and MBDL-NanoMat groups were 9.78, 4.21, 5.07, 4.01, and 2.94-fold higher than the MBDL-NanoMat + NIR group, respectively ($p < 0.05$) (Figure S20B, Supporting Information). This demonstrated that CDT/PTT/ferroptosis/cuproptosis effects by the HyPhil layer, along with the CT approach of RPM from the HyPhob layer, can provide a greater suppressive potential of 4T1 tumor spheroid growth under NIR light application.

Cellular ROS levels in 4T1 tumor spheroids were also quantitatively analyzed (Figure S21, Supporting Information). The fluorescence intensity indicating ROS levels in the MBDL-NanoMat

+ NIR group was significantly higher than those in the control, HyPhob, HyPhil, HyPhil + NIR, and MBDL-NanoMat groups ($p < 0.05$) (Figure S21B, Supporting Information). The combination effects of Cu NPs (from the HyPhil layer) and RPM (from the HyPhob layer) in MBDL-NanoMat seem to elevate the cellular ROS level with NIR light exposure.

The live/dead cellular assay was also performed to assess the cancer cell killing efficiency (Figure S22, Supporting Information). Calcein-AM represents the live cells (green intensity), while ethidium homodimer-1 (EthD-1) indicates the dead cells (red intensity). Compared to the control group, the MBDL-NanoMat + NIR group showed an 11.7% calcein-AM level, whereas its EthD-1 intensity was 7.33-fold higher value ($p < 0.05$) (Figure S22B, Supporting Information). It is expected that the combination of Cu NPs (from the HyPhil layer) and RPM (from the HyPhob layer) with NIR laser exposure can elevate 4T1 tumor spheroid-killing efficiency.

The tumor penetration capability of the developed MBDL-NanoMat was also tested in the 4T1 tumor spheroid model (Figure S23, Supporting Information). Rho B was incorporated into the MBDL-NanoMat as a fluorescent probe in this study, and a homogeneous distribution of red fluorescence signal was seen in the 4T1 tumor spheroid. Observed data suggest the efficient penetration of the drug-loaded MBDL-NanoMat system into the core section of 4T1 tumor spheroids.

2.5. In Vivo Anti-Recurrence Capabilities

Tumor recurrence, often driven by residual cancer cells that survive during initial treatments such as surgery, remains a significant challenge in cancer therapy. To address this, the current study investigated the potential of the designed MBDL-NanoMat to inhibit tumor recurrence, treat bacterial infections, and enhance wound healing using a TNBC mouse model (Figure 4). On day 1, after tumor dissection and *S. aureus* application, all the test groups were sutured with the NF mat systems. Moreover, tumor volume and wound size were monitored during the test period (Figure 4A). From day 11, the recurrent tumor volume began to increase significantly. The tumor volume for control, HyPhob, HyPhil, HyPhil + NIR, MBDL-NanoMat, and MBDL-NanoMat + NIR groups on day 11 indicated 25.69 ± 17.93 , 32.33 ± 20.28 , 10.09 ± 13.93 , 5.92 ± 10.85 , 0.6 ± 1.09 , and 0 mm^3 , respectively (Figure 4B). At the end of the experiment (day 14), the tumor volume for control, HyPhob, HyPhil, HyPhil + NIR, MBDL-NanoMat, and MBDL-NanoMat + NIR groups exhibited 164 ± 98.1 , 40.9 ± 35 , 93.1 ± 68.5 , 40.3 ± 39.7 , 7.6 ± 8.9 , and 0 mm^3 (Figure 4B). The tumor growth in the MBDL-NanoMat + NIR group was entirely suppressed compared to other groups, leading to the complete remission of TNBC (Figure 4B). The observed results are likely

upper left (UL), upper right (UR), and LR + UR panels are displayed. Data are shown as mean \pm SD ($n = 3$). * $p < 0.05$, between indicated groups. One-way ANOVA with Tukey's *post hoc* test. E) Intracellular GSH assay in 4T1 cells. Relative cellular GSH levels of the control, HyPhob, HyPhil, HyPhil + NIR, MBDL-NanoMat, and MBDL-NanoMat + NIR groups are plotted. Each point represents mean \pm SD ($n = 3$). One-way ANOVA with Tukey's *post hoc* test. F) Lipid ROS and MDA assays in 4T1 cells. Relative lipid ROS and MDA levels of the control, HyPhob, HyPhil, HyPhil + NIR, MBDL-NanoMat, and MBDL-NanoMat + NIR groups are plotted. Each point represents mean \pm SD ($n = 3-4$). * $p < 0.05$, between indicated groups. One-way ANOVA with Tukey's *post hoc* test. G) Western blot assay in 4T1 cells. Representative images of DLAT oligomer, DLAT, FDX1, LIAS, GPX4, and β -actin bands are shown ($n = 3$).

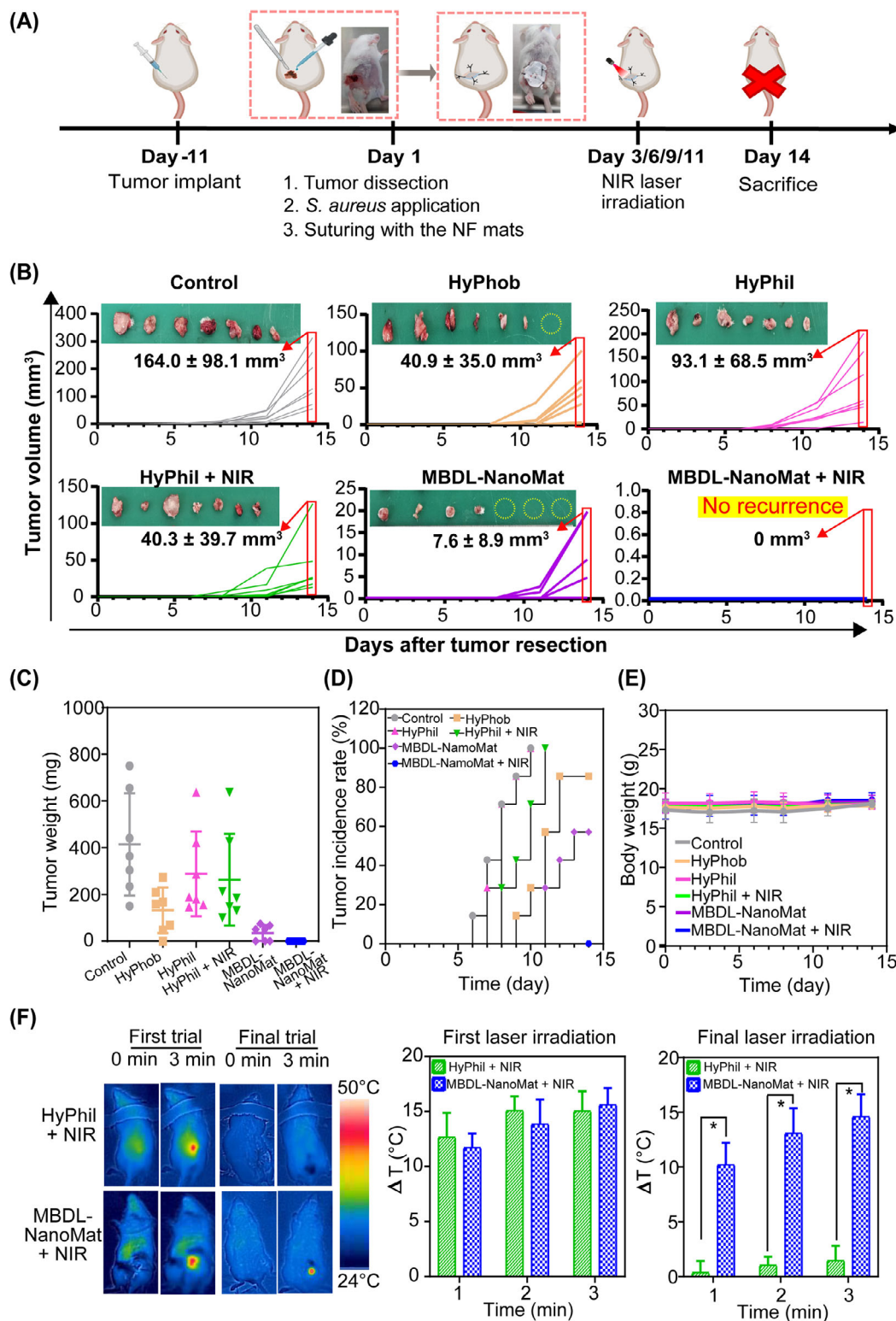


Figure 4. In vivo antitumor efficacy of the multifunctional MBDL-NanoMat system in 4T1 tumor-resected mouse models. A) Schematic of the tumor resection and bacterial infection model development and corresponding time schedule. B) Tumor volume profiles of control, HyPhob, HyPhil, HyPhil + NIR, MBDL-NanoMat, and MBDL-NanoMat + NIR groups ($n = 7$). C) Dissected tumor weight of control, HyPhob, HyPhil, HyPhil + NIR, MBDL-NanoMat, and MBDL-NanoMat + NIR groups. Mean and SD values are shown ($n = 7$). D) Tumor incidence rate profiles according to the time ($n = 7$). E) Body weight profiles of control, HyPhob, HyPhil, HyPhil + NIR, MBDL-NanoMat, and MBDL-NanoMat + NIR groups. Each point represents mean \pm SD ($n = 7$). F) Whole-body thermal images of HyPhil + NIR and MBDL-NanoMat + NIR groups in tumor-resected mouse models. Irradiation time-dependent temperature change profiles are presented. Each point represents mean \pm SD ($n = 7$). * $p < 0.05$, between indicated groups. Two-tailed t -test.

due to the combined CDT/PTT/ferroptosis/cuproptosis effects of Cu NPs (from the HyPhil layer) and the CT function of RPM (from the HyPhob layer). Importantly, NIR irradiation of the MBDL-NanoMat was crucial for enhancing anti-recurrence effects, as evidenced by the significantly improved outcomes compared to non-irradiated groups. The dissected tumor weight data also matched the tumor volume results (Figure 4B,C). The incidence of tumors (%) was investigated, and no occurrence was observed in the MBDL-NanoMat + NIR group throughout the test period (Figure 4D). On the final day, the mice exhibited negligible body weight change profiles, indicating systemic safety of the applied MBDL-NanoMat system (Figure 4E).

The photothermal ablation capability of the designed nanofibrous matrix was assessed by measuring temperature elevation at the sutured site during NIR laser irradiation (Figure 4F). During the initial trial of NIR laser irradiation, no significant difference was observed between the HyPhil + NIR and MBDL-NanoMat + NIR groups. However, by the final irradiation cycle, the MBDL-NanoMat + NIR group maintained a similar temperature elevation to that observed in the first trial, while the HyPhil + NIR group failed to exhibit any definite photothermal conversion effect. This was due to the rapid disintegration and dissolution properties of the HyPhil layer, which prevented it from being retained on the skin site for an extended period. In contrast, the MBDL-NanoMat provided sustained therapeutic effects under NIR laser exposure. Hyperthermia has been reported to be used alone or as an adjuvant therapy for tumor recurrence following surgery.^[27] It inhibits tumor recurrence by exploiting tumor cells' lower heat tolerance, raising the temperature to 39–45 °C to induce apoptosis and necrosis, and impair DNA repair, thereby suppressing its recurrence.^[27d] The designed MBDL-NanoMat exhibited a sufficient temperature elevation for effective PTT. Notably, temperature elevations remained below 50 °C, ensuring effective hyperthermia-induced cancer cell death without causing significant damage to the normal skin surrounding the tumor tissue.^[28] These findings collectively indicate that the application of the MBDL-NanoMat in combination with NIR light effectively and safely prevents tumor recurrence following the surgical removal of TNBC.

2.6. In Vivo Antibacterial and Wound Healing Functions

The post-operative wound healing potential of the MBDL-NanoMat was evaluated in a bacteria-infected mouse model (Figure 5A). The wound images and the corresponding quantitative analysis of the wound area (%) over the monitoring period are presented (Figure 5B,C). On day 3, the MBDL-NanoMat + NIR group exhibited a smaller mean wound size than the other groups. On day 7, the wound area in MBDL-NanoMat + NIR groups had significantly reduced, whereas the wound size data in control, HyPhob, HyPhil, HyPhil + NIR, and MBDL-NanoMat groups remained at 82.4%, 75%, 79.9%, 80.3%, and 79.6%, respectively. On day 14, the infected wound in the MBDL-NanoMat + NIR group was almost fully recovered (<5% of the remaining wound area). These findings indicate that the MBDL-NanoMat combined with NIR light application can completely recover *S. aureus*-infected wounds.

During the therapy process, the temperature of the MBDL-NanoMat + NIR group was <50 °C, which is considered safe for the surrounding skin tissues. To investigate the pathophysiological changes at the wound sites, tissue sections were subjected to hematoxylin and eosin (H&E) staining for general histological assessment, Masson's trichrome staining for collagen visualization, and immunofluorescence staining for the angiogenic markers such as vascular endothelial growth factor (VEGF) and platelet endothelial cell adhesion molecule-1 (CD31) (Figure 5D).^[29] H&E staining images revealed that the MBDL-NanoMat + NIR group led to the highest epidermal formation. Moreover, the MBDL-NanoMat + NIR group exhibited abundant newly formed hair follicles in dermal tissue. Masson's trichrome staining, which assesses collagen deposition, is crucial for tissue remodeling. The MBDL-NanoMat + NIR group had extensive collagen deposition (blue color), indicating a superior skin recovery rate compared to the other groups (Figure 5D; Figure S24A, Supporting Information) ($p < 0.05$). VEGF is essential for promoting the migration and proliferation of vascular endothelial cells and plays a crucial role in angiogenesis.^[6c,29b] CD31, a transmembrane protein highly expressed during early angiogenesis, is utilized to identify endothelial cells and serves as a critical marker for assessing angiogenic activity.^[6c,29b] Immunofluorescence staining images demonstrated that the MBDL-NanoMat + NIR group exhibited the highest levels of VEGF and CD31 compared to the other groups ($p < 0.05$) (Figure 5D; Figure S24B,C, Supporting Information). These findings revealed that the application of MBDL-NanoMat with NIR light exposure significantly upregulated the expression levels of VEGF and CD31, thus facilitating the wound-healing process. Collectively, histological analysis demonstrated that wounds treated with the MBDL-NanoMat combined with NIR laser irradiation following tumor surgery exhibited enhanced healing efficiency and accelerated wound recovery rate. In vivo, the antibacterial efficacy of the MBDL-NanoMat system was assessed by culturing microbes isolated from the injured skin tissues on LB agar plates (Figure 5E). Although all treatments demonstrated antibacterial effects, the MBDL-NanoMat + NIR group showed a significantly lower CFU value (approaching zero) compared to the control, HyPhob, HyPhil, HyPhil + NIR, and MBDL-NanoMat groups. This complete inhibition of bacterial growth by the MBDL-NanoMat + NIR group highlights the potential of the MBDL-NanoMat combined with NIR laser irradiation as a highly effective approach for combating bacterial infections, thereby accomplishing accelerated wound recovery following cancer surgery.

2.7. Systemic Safety

The biosafety of the designed MBDL-NanoMat was evaluated in mice by hematological and histological tests (Figures S25,S26, Supporting Information). Hepatotoxicity and renal toxicity were evaluated through a blood biochemistry assay (Figure S25, Supporting Information). Although a modest reduction in blood urea nitrogen (BUN) levels was observed in the MBDL-NanoMat + NIR group relative to the control group, the BUN levels in both groups fell within the established normal range for this parameter.^[30] There were no significant differences among all tested groups in albumin, aspartate transaminase (AST), and

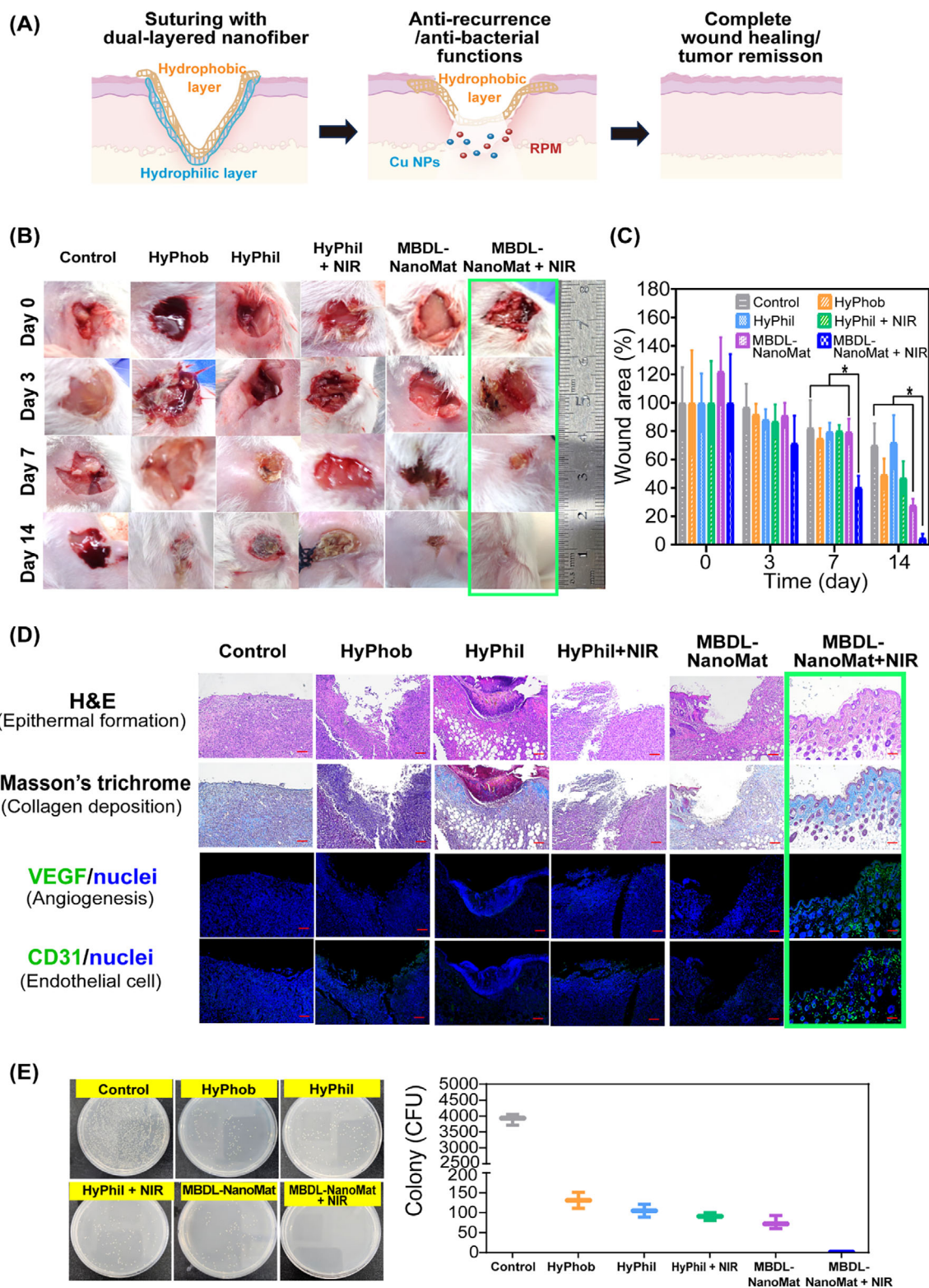


Figure 5. In vivo wound healing potential of nanofibrous systems in the bacteria-infected mouse model. A) Rationales for the fabrication of MBDL-NanoMat systems for anti-recurrence and wound healing applications. B) Photographs of wounds treated with HyPhob, HyPhil, HyPhil + NIR, MBDL-NanoMat, and MBDL-NanoMat + NIR groups on days 0, 3, 7, and 14. C) Changes in wound area (%) after suturing with nanofibrous matrix. Each point represents mean \pm SD ($n = 7$). * $p < 0.05$, between indicated groups. One-way ANOVA with Tukey's *post hoc* test. D) Microscopic images of H&E, Masson's trichrome, and immunofluorescence staining (VEGF and CD31) in skin tissues. E) Images of colonies of *S. aureus* derived from wound tissues. The number of CFU is plotted. Each point represents mean \pm SD ($n = 3$).

alanine transaminase (ALT) levels (Figure S25, Supporting Information). This suggests that the designed MBDL-NanoMat can maintain normal hepatic and renal functions comparable to the control (no treatment) group. No significant treatment-related pathological changes were observed in the heart, kidney, liver, lung, or spleen of mice treated with the nanofibrous matrix, as evidenced by H&E staining (Figure S26, Supporting Information). This lack of histopathological abnormalities indicates that the MBDL-NanoMat does not induce systemic toxicity when applied at the wound site. These findings underscore the safety and biocompatibility of the MBDL-NanoMat for its intended use in preventing tumor recurrence and promoting wound healing.

3. Conclusion

This work introduces a transformative approach to post-surgical cancer care, showcasing how rationally designed nanofibrous matrices can effectively address the dual challenges of tumor recurrence prevention and wound healing. By integrating advanced therapeutic modalities within a single biomaterial construct, this multi-functional platform underscores the potential of precision-engineered scaffolds to meet complex post-surgical demands in a targeted and efficient manner. The system's capacity to combine multiple anticancer mechanisms—such as CT, CDT, PTT, ferroptosis, and cuproptosis—while maintaining excellent biocompatibility highlights its versatility and sophistication. These attributes position it as a promising candidate for clinical translation in TNBC treatment.

Furthermore, the rational design of the bilayer matrix, which integrates rapid-release functionality with sustained therapeutic delivery, provides a model for addressing key limitations of conventional cancer therapies, including incomplete tumor eradication and extended wound recovery. The platform's capacity to enhance angiogenesis, promote dermal regeneration, and prevent bacterial infections further highlights its multifunctional nature, making it particularly advantageous for applications in complex surgical settings.

Beyond the immediate findings, the design principles and fabrication strategies detailed in this study have broader implications for the field of nano-biomaterials development. This work offers valuable insights into the creation of next-generation therapeutic platforms by specifically addressing the often-neglected interplay between cancer recurrence and wound healing. Such insights can guide the development of analogous multifunctional biomaterials for diverse oncological contexts, such as metastasis-prone cancers, recurrent tumor surgeries, or chronic wounds arising from cancer therapies. Moreover, the inherent adaptability of this approach may foster new opportunities for personalized medicine, enabling the customization of biomaterials to meet the unique needs of individual patients and specific clinical scenarios.

In conclusion, the innovative multifunctional bioactive dual-layered nanofibrous matrix (MBDL-NanoMat) developed in this study presents a new method for the design of advanced biomaterials, providing a powerful and versatile platform for post-surgical cancer care. The matrix's ability to integrate various therapeutic modalities, support tissue regeneration, and prevent complications while ensuring safety and biocompatibility signi-

fies a substantial advancement in the fields of oncology and regenerative medicine.

4. Experimental Section

Materials: PCL (MW: 80 kDa), gelatin (gel strength: ≈ 225 g Bloom, Type B), citric acid, copper(II) chloride dihydrate, Rho B, trifluoroethanol (TFE), 2-thiobarbituric acid (TBA), 2',7'-dichlorofluorescein diacetate (DCFH-DA), 3,3',5,5'-tetramethylbenzidine dihydrochloride hydrate (TMB DH), and DTNB were supplied by Sigma-Aldrich (Saint Louis, MO, USA). PVP and 1,8-octanediol were purchased from Tokyo Chemical Industry Co. Ltd. (Tokyo, Japan). RPM was acquired from LC Labs (Woburn, MA, USA).

Fabrication of the MBDL-NanoMat: Cu NPs were synthesized by the reaction of CuCl_2 , H_2O_2 , and NaOH with a slight modification.^[8a] PVP (0.5 g) was dissolved in an aqueous solution containing $\text{CuCl}_2 \cdot 2\text{H}_2\text{O}$ (5 mL, 0.01 M). NaOH (5 mL, 0.02 M) was added to the above solution, and H_2O_2 (30%, 100 μL) was dropwise added to the mixture. The products were gathered by spinning them in a centrifuge at a force of 42 000 g for 30 min after stirring for 30 min. They were then washed three times with distilled water (DW). Particle shape and mean diameter of Cu NPs were measured by TEM (JEM-2100F, JEOL Ltd., Tokyo, Japan). The particle size and zeta potential of Cu NPs were analyzed using an ELS-Z1000 particle size and zeta potential analyzer (Otsuka Electronics, Tokyo, Japan). Cu NPs dispersion was irradiated with NIR light (808 nm, 0.5 W cm^{-2}) for 3 min. The temperature change in each group was recorded by a thermal camera (FLIR E8, FLIR Systems, Inc., Wilsonville, OR, USA).

POC was synthesized by the reaction of citrate and 1,8-octanediol. Citric acid (384 mg) and 1,8-octanediol (233.6 mg) were placed in a three-neck round bottom flask and incubated at 160 °C for 20 min. The temperature was then reduced to 140 °C, and the reaction proceeded for 1 h. Afterward, 60% ethanol was added and precipitation was induced by adding DW. A freeze-drying process was employed to prepare the samples for further use.

POC (10 mg) was dissolved in DMSO- d_6 (1 mL) and verified with ^1H NMR spectroscopy (Avance Neo 600, Bruker Ltd., Billerica, MA, USA). For MW analysis of POC, POC (5 mg) was dissolved in tetrahydrofuran (2 mL) and measured by GPC (Acquity APC, Waters Corp., Milford, MA, USA).

To prepare different ratios of PCL/gelatin (PG) NF, PCL was dissolved in a dichloromethane (DCM)/dimethyl formamide (DMF) mixture (v/v, 9:1), while gelatin was dissolved in TFE. Each component was then mixed according to the specified ratios. To prepare different ratios of PCL/POC/gelatin (PPG) NF, a mixture of DCM and DMF (in a 9:1 volume ratio) was used to dissolve PCL and POC, while TFE was used to dissolve gelatin. The various components were mixed together in the ratios that were assigned to each. The syringe was filled with the mixture using a stainless-steel needle (25 G). The flow rate was consistently 1 mL h^{-1} , and an electric field strength of 25 kV was applied. The tensile strength and elongation values of PCL NF, PG NF, and PPG NF were assessed using a universal testing machine (QM100S, Qmesys, Uiwang, Republic of Korea) with a 10 mm min^{-1} speed and a 50 N load cell.

The fabrication of the MBDL-NanoMat began with the preparation of the HyPhil layer, which was composed of a mixture of gelatin and Cu NPs (GC). Gelatin (30 mg) was dispersed in 0.8 mL of TFE, and the dispersion of Cu NPs (10 mg mL^{-1} in deionized water, 0.2 mL) was thoroughly mixed with the gelatin dispersion. The GC mixture was then loaded into a syringe fitted with a 21 G stainless-steel needle. A constant flow rate of 0.5 mL h^{-1} was maintained, with an applied electric field strength of 25 kV. The syringe was positioned vertically, 10 cm above the collector's surface. For the fabrication of the HyPhob layer, a mixture of PCL, POC, and RPM, referred to as the PPR mixture, was prepared. PCL (70 mg) was dispersed in a 0.8 mL solution of DCM and DMF (v/v, 9:1), followed by the addition of RPM (5 mg), which was dissolved under mechanical stirring. Subsequently, 0.2 mL of a POC dispersion (10 mg mL^{-1} in the DCM/DMF mixture) was added to the solution. This PPR mixture was also loaded into a syringe with a 21 G needle, with a constant flow rate of 1 mL h^{-1} and an

electric field strength of 18 kV. The syringe was positioned vertically, 15 cm above the collector's surface. The PPR mixture was electrosprayed directly onto the previously formed HyPhil layer. Finally, the MBDL-NanoMat was incubated at 40 °C for 24 h to ensure complete drying.

Physicochemical Assessment of the MBDL-NanoMat: NF was electrosprayed in a time-dependent manner (for 1, 2, and 4 h), and their thickness was measured using a profilometer (Alpha-Step D-500 Stylus profilometer, KLA Corp., Milpitas, CA, USA). Mice were sutured with NF mats of varying thickness, and whole-body thermal images were taken during 3 min of NIR laser irradiation (808 nm, 0.5 W cm⁻²).

The hydrophilicity and hydrophobicity of HyPhil and HyPhob were evaluated via testing the WCA. A water droplet (3 µL) was put on the nanofibrous matrix (3 cm × 3 cm), and WCA was measured by the contact angle measuring system (DSA100, Kruss, Hamburg, Germany).

The morphology of MBDL-NanoMat (in lateral and folded views) was measured by a variable pressure-field emission-scanning electron microscope (VP-FE-SEM, JSM-7900F, JEOL Ltd.). To accurately measure each layer (HyPhil and HyPhob) on the folded side of the NF matrix, the HyPhil side was selectively stained with Rho B. Before imaging, each specimen was coated with gold (Au) under the vacuum conditions, and images were captured. The average diameter of the NF in each layer was quantified using ImageJ software.^[31] The elemental composition of the HyPhil layer was analyzed using SEM coupled with EDS.

The content of RPM in the HyPhob layer was determined by high-performance liquid chromatography (HPLC) analysis. The mobile phase was composed of DW (including 0.1% phosphoric acid) and acetonitrile (including 0.1% phosphoric acid) (10:90, v/v). The reverse phase C18 column (Kinetex, 250 mm × 4.6 mm, 5 µm; Phenomenex, Torrance, CA, USA) was connected to the HPLC system (Agilent 1260 Infinity II, Agilent Technologies, Santa Clara, CA, USA) and the flow rate was set as 1 mL min⁻¹. The injection volume of each sample was 10 µL, and chromatograms were monitored at 205 nm. The entrapment efficiency of Cu NPs in the HyPhil layer was determined by an inductively coupled plasma optical emission spectrometer (ICP-OES; Agilent 5900, Agilent Technologies). The HyPhil sample was pre-treated with nitric acid prior to ICP-OES analysis.

XRD profiles of Cu NPs, HyPhil, RPM, and HyPhob groups were measured by D8 ADVANCE with DAVINCI (Bruker AXS GmbH, Karlsruhe, Germany) and LYNXEYE detector. The electrosprayed NF membranes were measured with CuK_α radiation in the 2θ range of 10–80° (for Cu NPs and HyPhil) and 10–50° (RPM and HyPhob) at 40 mA and 40 kV.

The WVP values of the Gauze, HyPhil, HyPhob, and MBDL-NanoMat samples were evaluated using a modified version of ASTM E96-00 (American Society for Testing and Materials, 2016). A dry and clean wet flask was filled with water (25 mL). Each specimen was positioned at a distance of 10 mm from the surface of the water in the flask. The weight of the wet flask and the specimen (W₀) was weighed. Subsequently, the wet flask was placed in an incubator at 37 ± 2 °C. After 24 h, the total weight of the wet flask and the specimen (W_t) was weighed, and the water permeability was determined using the following equation:

$$P = \frac{W_0 - W_t}{S} \quad (1)$$

where *P* represents the water vapor permeability (g m⁻² day⁻¹), *W*₀ – *W*_t denotes the change in mass of the sample after 24 h and *S* represents the permeation area (m²).^[32]

The FT-IR spectra of the Cu NPs, gelatin, PCL, PCL/POC, HyPhil, and HyPhob specimens were obtained using an FT-IR spectrometer (Frontier, PerkinElmer Inc., Waltham, MA, USA). The attenuated total reflectance mode was used to measure transmittance values in the range of 400–4000 cm⁻¹.

Tensile strength and elongation of HyPhil, HyPhob, and MBDL-NanoMat groups were evaluated by a universal testing machine (QM100S, Qmesys, Uiwang, Republic of Korea) at a speed of 10 mm min⁻¹ with 50 N load cell.

To assess the adhesion properties of the designed nanofibrous matrix, the mice skin tissue (BALB/c mouse, female, ≈20 g of body weight; Koatech Inc., Pyeongtaek, Republic of Korea) was incubated in PBS for 4 h be-

fore applying the MBDL-NanoMat. Adhesion was assessed by measuring the time that the MBDL-NanoMat remained attached under different applied weights. Elongation was evaluated using a universal testing machine, with the NF adhered to skin tissue, to determine the extent of stretching.

The attachment between the skin and MBDL-NanoMat was confirmed using FT-IR spectroscopy and XPS (K-Alpha+, Thermo Fisher Scientific, Waltham, MA, USA). XPS was also employed to determine the atomic composition of the nanofibrous matrix, analyzing the binding energies (BE) of carbon, nitrogen, oxygen, and copper.

The assessment of wetting capability was conducted using the reported technique.^[24b,33] A dish with a diameter of 150 mm was filled with pH 6.5 buffer solution and filter papers with a diameter of 110 mm (sourced from CHMLAB group, Barcelona, Spain) were positioned on the surface to saturate them. Subsequently, each specimen (2 cm × 2 cm) of HyPhil, HyPhob, and MBDL-NanoMat groups was applied to the papers, and images were captured at specified intervals.

The disintegration assessment of MBDL-NanoMat was conducted using a disintegration tester (TD-20S, Campbell Electronics, Mumbai, India).^[24b,33] Each specimen (2 cm × 2 cm) was placed into the designated basket and submerged in PBS (pH 6.5, 1 L) at 37 ± 2 °C. They moved in repeated vertical movements, with photographic images taken at the pre-determined time. The remaining MBDL-NanoMat mats were collected and lyophilized for weight measurement.

Released amounts of Cu NPs from the nanofibrous matrix were measured by ICP-OES analysis. Each specimen was immersed in PBS (pH 6.5, 10 mL) and obtained at predetermined times (10, 30, 45, and 60 s). Before measurement, all the obtained samples were treated with nitric acid.

Released amounts of RPM from the nanofibrous matrix (2 cm × 2 cm) were assessed in PBS (pH 6.5, 10 mL) containing 0.3% sodium dodecyl sulfate (SDS). The released medium (0.2 mL) was acquired at 2, 6, 24, 48, 72, 120, 144, 168, 192, and 240 h and replenished with the same volume of release media. The released RPM was determined by the described HPLC analysis.

The photothermal effect of the MBDL-NanoMat was studied using an NIR diode laser (808 nm wavelength). To evaluate the in vitro photothermal transducing effect, HyPhil, HyPhob, and MBDL-NanoMat were exposed to NIR light (808 nm, 0.5 W cm⁻²) for 3 min. The temperature change in each group was recorded using a thermal camera.

For the extracellular hydroxyl radical production ability of Cu NPs, the TMB method was introduced at different pH (pH 7.4 and 5.5). Cu NPs dispersion (0.2 mg mL⁻¹, 0.5 mL) was mixed with TMB DH (1.5 mg⁻¹ mL, 0.5 mL), and samples were collected at 0, 30, 60, and 120 min after incubation. The absorbance at 650 nm was detected by a microplate reader. H₂O₂ solution with different concentrations (1, 2.5, 5, and 25 µM; 1 mL) was added to the TiOSO₄ solution (1 mg mL⁻¹, 1 mL). Cu NPs (1 mg mL⁻¹ in DW) were mixed with the TiOSO₄ solution (1 mg mL⁻¹, 1 mL). UV-vis spectra of different mixtures were measured, and a plot of absorbance was obtained based on the different absorbances at 405 nm wavelength.

The generation of hydroxyl radicals from the designed NF mats was investigated by TMB-based assay in the presence or absence of GSH or NIR laser irradiation. Each specimen (1 cm × 1 cm) of HyPhil, HyPhob, and MBDL-NanoMat was prepared and dispersed in PBS (pH 6.5, 0.5 mL). The NIR laser (808 nm, 0.5 W cm⁻²) was irradiated for 3 min. It was then blended with a 5 mM TMB solution (0.4 mL) for the reaction. The samples were incubated at 37 °C, and the supernatant (0.2 mL) was measured at 650 nm at 0, 5, 10, 30, and 60 min. Absorbance values were detected at 650 nm using a microplate reader (SpectraMax i3, Molecular Devices, Sunnyvale, CA, USA).

ESR analysis was conducted to verify the generation of hydroxyl radicals from the designed NF.^[34] HyPhil, HyPhob, and MBDL-NanoMat samples (1 cm × 1 cm) were placed in tubes containing 0.5 mL of PBS (pH 6.5). The NIR laser (808 nm, 0.5 W cm⁻²) treatment group was irradiated for 3 min. Subsequently, 0.5 mL of DMPO solution (100 mM) was added to each tube. After 30 min incubation at 37 °C, the samples were analyzed using an ESR spectrometer (JES-X320, JEOL Ltd.).

Each specimen (1 × 1 cm) was prepared and placed in a conical tube. GSH solution (0.185 mg mL⁻¹; 4 mL) was added to each tube, and the tubes were incubated at 37 °C for 60 min. Then, DTNB solution

(0.119 mg mL⁻¹; 4 mL) was added, and the tubes were incubated at 37 °C for an additional 10 min. Each specimen was then diluted with DW and the absorbance at 250–600 nm was measured using UV–vis spectrometer (Libra S80 double beam spectrophotometer, Biochrom Ltd., Cambridge, UK).

In Vitro Anticancer Efficacy Tests: The antiproliferative effect of the engineered nanofibrous matrix on 4T1 cells was assessed. 4T1 cells were acquired from the American Type Culture Collection (Manassas, VA, USA). A mixture of RPMI 1640 medium, penicillin–streptomycin (1%, v/v), and FBS (10%, v/v) was used for the culture of 4T1 cells. 4T1 cells were seeded in a 96-well plate at a density of 5×10^3 cells per well and incubated at 37 °C with 5% CO₂ for 24 h. HyPhob, HyPhil, and MBDL-NanoMat (1 × 1 cm) were incubated in a media and collected at certain times. HyPhil was collected after 5 to 60 s, HyPhob after 24 to 144 h, and MBDL-NanoMat was collected at both times. The prepared samples were applied to the cells and incubated for 24 h. After incubating with the samples for 4 h, the cells were exposed to NIR laser irradiation (808 nm, 0.5 W cm⁻²) for 5 min. The cells were treated using the CellTiter 96 Aqueous One Solution Cell Proliferation Assay Reagent (Promega Corp., Fitchburg, WI, USA) following the manufacturer's recommended protocol. Absorbance for each group was then measured at 490 nm using a microplate reader.

The level of cellular ROS was measured using DCFH-DA. 4T1 cells were seeded in a 6-well plate at a density of 2×10^6 cells per well. The samples were prepared as follows: HyPhob, HyPhil, and MBDL-NanoMat (1 × 1 cm) were incubated in media, and the media samples were collected at specific time points (96 h for HyPhob, 30 s for HyPhil, and MBDL-NanoMat for 30 s and 96 h and consequent blending). The cells were treated with the obtained samples (1 mL) of HyPhob, HyPhil, and MBDL-NanoMat and incubated for 24 h with or without exposure to NIR light (808 nm, 0.5 W cm⁻², and 5 min). Following washing with cold PBS, DCFH-DA (10 μM) was added to the cells and incubated for 20 min. Fluorescence intensity was then analyzed using a flow cytometer (FACSVerse, BD Biosciences, Franklin Lakes, NJ, USA).

The ability of the developed nanofibrous matrix to induce apoptosis in 4T1 cells was examined. 4T1 cells were seeded in a 6-well plate at a density of 2×10^6 cells per well and cultured for 24 h. The samples were prepared as follows: HyPhob, HyPhil, and MBDL-NanoMat (1 × 1 cm) were incubated in media, and the media samples were collected at specific time points (96 h for HyPhob, 30 s for HyPhil, and MBDL-NanoMat for 30 s and 96 h and consequent blending). The obtained samples (1 mL) of HyPhob, HyPhil, and MBDL-NanoMat were then applied to the cells with NIR light (808 nm, 0.5 W cm⁻², and 5 min) and incubated for 6 h. The FITC Annexin V Apoptosis Detection Kit (BD Pharmingen, BD Biosciences) was utilized to assess the efficacy of apoptosis induction using a flow cytometer.

Relative cellular GSH level was measured by the colorimetric method.^[24] 4T1 cells were loaded onto a 6-well plate at 2×10^6 cells per well and they were incubated for 24 h. The samples were prepared as follows: HyPhob, HyPhil, and MBDL-NanoMat (1 × 1 cm) were incubated in media, and the media samples were collected at specific time points (96 h for HyPhob, 30 s for HyPhil, and MBDL-NanoMat for 30 s and 96 h and consequent blending). The obtained samples (1 mL) of HyPhob, HyPhil, and MBDL-NanoMat were treated with or without NIR laser (808 nm, 0.5 W cm⁻², and 5 min) and incubated for 6 h. Then, each specimen was eliminated, and the cells were rinsed with cold PBS for twice. Cell lysates were obtained by repeated freezing-thawing procedures. The Glutathione Colorimetric Detection Kit (Thermo Fisher Scientific, Inc.) was used to measure cellular GSH levels with a microplate reader.

To evaluate the LPO of 4T1 cells with a nanofibrous matrix, BODIPY 581/591 C11 was used.^[35] 4T1 cells were seeded in a 6-well plate at a density of 2×10^6 cells per well and cultured for 24 h. The samples were prepared as follows: HyPhob, HyPhil, and MBDL-NanoMat (1 × 1 cm) were incubated in media, and the media samples were collected at specific time points (96 h for HyPhob, 30 s for HyPhil, and MBDL-NanoMat for 30 s and 96 h and consequent blending). The obtained samples (1 mL) of HyPhob, HyPhil, and MBDL-NanoMat (1 × 1 cm) were treated with or without NIR laser (808 nm, 0.5 W cm⁻², and 5 min) was added to the cells and further cultured for 6 h. After eliminating the cell culture media, cells were washed with cold PBS, BODIPY 581/591 C11 (10 μM) solution

was added to the cells and incubated for 30 min. The oxidation of BODIPY 581/591 C11 in the cell was estimated by a flow cytometer.

To determine MDA levels, 4T1 cells were plated in 6-well plates at a density of 5×10^5 cells per well and cultured for 24 h. The samples were prepared as follows: HyPhob, HyPhil, and MBDL-NanoMat (1 × 1 cm) were incubated in media, and the media samples were collected at specific time points (96 h for HyPhob, 30 s for HyPhil, and MBDL-NanoMat for 30 s and 96 h and consequent blending). The acquired samples (1 mL) of HyPhob, HyPhil, and MBDL-NanoMat (1 × 1 cm) were applied to the cells and incubated for 6 h. The cells were lysed using DPBA (100 μL) with an ultrasonic processor for 15 s on ice. Subsequently, the lysates were centrifuged at 16 100 g for 10 min and the supernatant was collected. The sample (50 μL) was added to the 0.1% phosphoric acid (400 μL) and 0.6% TBA (100 μL) at 90 °C for 30 min. The fluorescence intensity was measured at an excitation/emission wavelength of 532/553 nm with the microplate reader.

4T1 cells were seeded into 6-well plates at 5×10^5 cells per well in 2 mL of complete cell culture media and incubated at 37 °C for 24 h. The samples were prepared as follows: HyPhob, HyPhil, and MBDL-NanoMat (1 × 1 cm) were incubated in media, and the media samples were collected at specific time points (96 h for HyPhob, 30 s for HyPhil, and MBDL-NanoMat for 30 s and 96 h and consequent blending). Then, cells were treated with the obtained samples (1 mL) of HyPhob, HyPhil, and MBDL-NanoMat (1 × 1 cm) for 6 h. Subsequently, the cells were washed with PBS for three times and lysed with radioimmunoprecipitation assay buffer. The protein concentration of cell lysates was measured by a BCA protein assay kit (Pierce, Rockford, IL, USA). Total proteins (10 μg) for each specimen were analyzed by sodium dodecyl sulfate-polyacrylamide gel electrophoresis (10% or 15%) and the proteins in the gel were transferred to polyvinylidene fluoride membranes. The membranes were blocked with 0.5% skimmed milk, including 0.1% Tween 20 for 1 h. FDX1 (1:2000, abcam, Cambridge, UK), LIAS (1:5000, Proteintech Group, Inc., Rosemont, IL, USA), DLAT (1:5000, Santa Cruz Biotechnology, Inc., Dallas, TX, USA), GPX4 (1:1000, abcam), and β-actin (1:10 000, Santa Cruz Biotechnology, Inc.) of primary antibody were incubated at 4 °C overnight and followed with secondary antibody (anti-rabbit IgG and anti-mouse IgG) labeled with horseradish peroxidase for 1 h. The enhanced chemiluminescence signal was collected for quantitative analysis of biomarkers.

In Vitro Antibacterial Test: *S. aureus* (Korean Collection for Type Cultures) was obtained from the Korea Research Institute of Bioscience and Biotechnology (Daejeon, Republic of Korea) in this study. This bacterium was subcultured in a nutrient agar (NA) plate at 37 °C for 24 h. Before the experiment, *S. aureus* was cultured in nutrient broth at 37 °C in a shaking incubator, 150 rpm for 18 h. Subsequently, it was diluted and cultured again at 37 °C in a shaking incubator for 4 h. The bacterial suspensions were diluted to 10⁶ CFU mL⁻¹. CFU was determined by measuring the optical density (OD) at 600 nm, where an OD is approximately equivalent to 5×10^{12} CFU mL⁻¹. The bacterial suspension was diluted to 10⁶ CFU mL⁻¹. The bacterial dilution (50 μL) was treated with the nanofibrous matrix of HyPhob, HyPhil, HyPhil + NIR, MBDL-NanoMat, and MBDL-NanoMat + NIR (2 mg mL⁻¹, 50 μL) on NA plate and incubated at 37 °C. The NIR-treated group was irradiated for 5 min at 0.5 W cm⁻². After 24 h, the number of bacterial colonies on NA agar plates was counted. For showing antibacterial activity (%), the broth dilution method was introduced for Cu NPs (0, 3.125, 6.25, 12.5, 25, and 50 μg mL⁻¹) and RPM (0, 25, 50, 100, 250, and 500 μg mL⁻¹) at different concentrations.

In Vitro Anticancer Activity Tests in a 3D Spheroid Model: To generate spheroids, 4T1 cells (2.4×10^5 cells per well) were seeded in AggreWell400 plates (24-well plate, STEMCELL Technologies Inc., Vancouver, Canada) and incubated for 24 h. The 4T1 tumor spheroids were then cultured for 4 days. Spheroid volume (V, mm³) was calculated using the formula: $V = 0.5 \times (\text{longest diameter}) \times (\text{shortest diameter})^2$. HyPhob, HyPhil, and MBDL-NanoMat samples (nanofibrous matrix, 1 cm × 1 cm) with or without NIR laser (0.5 W cm⁻² and 5 min) were applied to the spheroids, and the spheroid volume was measured.

To assess ROS levels in 4T1 tumor spheroids, DCFH-DA was used as a detection probe. Nanofibrous matrix specimens (1 cm × 1 cm) of HyPhob, HyPhil, and MBDL-NanoMat were treated to the spheroids with or

without NIR light (0.5 W cm^{-2} and 5 min) and incubated for 4 days. For ROS detection, DCFH-DA ($10 \mu\text{M}$) was added to the spheroids and incubated for 30 min. Afterward, the spheroids were washed three times with cold PBS. ROS levels were observed using an inverted fluorescence microscope (Eclipse Ts2, Nikon, Tokyo, Japan).

To quantify the proportion of live and dead cells within 4T1 tumor spheroids, nanofibrous matrix specimens ($1 \text{ cm} \times 1 \text{ cm}$) of HyPhob, HyPhil, and MBDL-NanoMat were treated to the spheroids with or without NIR laser (0.5 W cm^{-2} and 5 min) and incubated for 4 days. The spheroids were then stained with calcein-AM ($2 \mu\text{M}$) to indicate live cells and EthD-1 ($4 \mu\text{M}$) to mark dead cells for 30 min. After washing three times with cold PBS, green and red fluorescence signals were quantitatively analyzed by using a fluorescence microscope.

To assess the penetration ability of the NF in 4T1 tumor spheroids, Rho B-loaded MBDL-NanoMat was prepared by incorporating Rho B into the HyPhil layer during fabrication, with the same procedures of all other manufacturing steps. After incubation for 24 h, the distribution of Rho B (corresponding to $5 \mu\text{g mL}^{-1}$ Rho B) within the 4T1 spheroids was evaluated by measuring the cellular fluorescence signal using confocal laser scanning microscopy (CLSM; LSM 880; Carl Zeiss, Thornwood, NY, USA).

In Vivo Anticancer, Antibacterial, and Wound Healing Studies: 4T1 cell suspension (2.5×10^5 cells in 0.05 mL) was injected into the mammary fat pad of BALB/c mouse (female, $\approx 20 \text{ g}$ of body weight; Koatech Inc.). After reaching the diameter of 5–7 mm, most tumor mass (1–2 mm) was resected according to the previous reports.^[36] Subsequently, $10 \mu\text{L}$ of Gram-positive *S. aureus* at a concentration of $1 \times 10^4 \text{ CFU mL}^{-1}$ was applied to the wound area where the tumor had been excised. The developed MBDL-NanoMat ($2 \times 2 \text{ cm}$, HyPhil layer for facing the tumor resection site) was sutured to the tumor resection site. Mice were divided into six groups: control, HyPhob, HyPhil, HyPhil + NIR, MBDL-NanoMat, and MBDL-NanoMat + NIR. NIR laser (808 nm , 0.5 W cm^{-2}) was irradiated for 3 min. Following suturing with the nanofibrous matrix, the tumor volume was measured on days 1, 3, 6, 9, 11, and 14. On the end of the experiment, tumor tissues were collected and weighed. For an antibacterial test, the tissue near the wound was taken and then cultured on LB agar plates to evaluate the antibacterial activity. Besides, the skin wounds were harvested and fixed in 4% formaldehyde before being embedded in paraffin. Furthermore, the paraffin blocks were cut into 5 mm thickness sections with a microtome before implementing H&E and Masson's trichrome stainings. Subsequently, immunofluorescence staining was performed by using the primary antibodies of CD31/PECAM-1 (D8V9E, Cell Signaling Technology, Danvers, MA, USA) and VEGF (S04-6D7, Novus Biologicals, Centennial, CO, USA) according to standard protocols. All animal studies were approved by the Animal Care and Use Committee of the Kangwon National University (KW-240207-1). Those animal studies were done with the National Institutes of Health (NIH) guide for the care and use of laboratory animals (NIH Publications No. 8023, revised 1978).

The in vivo safety of nanofibrous matrix in mice was investigated through blood chemistry and H&E staining assays. On the end of the experiment, blood samples were collected via the retro-orbital sinus/plexus method and the serum levels of albumin, BUN, AST, and ALT were measured using an AU480 chemistry analyzer (Beckman Coulter, Brea, CA, USA). The major organs (i.e., heart, kidney, liver, lung, and spleen) were extracted from the mice and preserved in a 4% formaldehyde. These tissues were subsequently dehydrated and processed with the H&E staining protocol.

Statistical Analysis: Statistical significance was determined using a two-tailed Student's *t*-test for comparisons between two groups and a one-way analysis of variance (ANOVA) with *post hoc* (Tukey) for comparisons involving more than two groups (Prism, GraphPad Software, Boston, MA, USA). Each experiment was repeated at least three times ($n \geq 3$), and the results were expressed as mean \pm standard deviation (SD). *P*-value less than 0.05 was regarded as statistically significant.

Supporting Information

Supporting Information is available from the Wiley Online Library or from the author.

Acknowledgements

This research was supported by the National Research Foundation of Korea (NRF) grant funded by the Ministry of Science and ICT and Ministry of Education (RS-2018-NR031068, 2020R1C1C1003945, and RS-2024-00352515) and Korea Basic Science Institute (National Research Facilities and Equipment Center) grant funded by the Ministry of Education (2022R1A6C101A739). K.-B.L. acknowledges the partial financial support from NIH R01 (1R01NS130836-01A1), NIH RM1 (RM1 NS133003-01), NIH R21 (R21 NS132556-01), Alzheimer's Association (AARG-NTF-21-847862), CDMRP (OCRP, OC220235P1), and NJ Commission on Cancer Research (COCR23PPR007).

Conflict of Interest

The authors declare no conflict of interest.

Data Availability Statement

The data that support the findings of this study are available from the corresponding author upon reasonable request.

Keywords

bacteria-infected wound treatment, chemodynamic therapy (CDT), dual-layered nanofibrous matrix, ferroptosis and cuproptosis, multifunctional biomaterials, photothermal therapy (PTT), triple-negative breast cancer (TNBC)

Received: January 17, 2025

Revised: April 15, 2025

Published online:

- [1] a) N. M. Almansour, *Front. Mol. Biosci.* **2022**, 9, 836417; b) R. A. Leon-Ferre, M. P. Goetz, *BMJ* **2023**, 381, 071674.
- [2] B. S. Yadav, P. Chanana, S. Jhamb, *World J. Clin. Oncol.* **2015**, 6, 252.
- [3] a) E. Donnelly, M. Griffin, P. E. Butler, *Ann. Biomed. Eng.* **2020**, 48, 9; b) Y. Shi, M. Zhou, S. Zhao, H. Li, W. Wang, J. Cheng, L. Jin, Y. Wang, *Mater. Des.* **2023**, 227, 111778.
- [4] P. A. van der Eerden, P. J. F. M. Lohuis, A. A. M. Hart, W. C. Mulder, H. Vuyk, *Plast. Reconstr. Surg.* **2008**, 122, 1747.
- [5] J. P. Totty, J. W. E. Moss, E. Barker, S. J. Mealing, J. W. Posnett, I. C. Chetter, G. E. Smith, *Int. Wound J.* **2020**, 18, 261.
- [6] a) S. Chen, S. K. Boda, S. K. Batra, X. Li, J. Xie, *Adv. Healthcare Mater.* **2018**, 7, 1701024; b) Y. K. Fu, X. Li, Z. H. Ren, C. Mao, G. Han, *Small* **2018**, 4, 1801183; c) Y. Xi, J. Ge, M. Wang, M. i Chen, W. Niu, W. Cheng, Y. Xue, C. Lin, B. o Lei, *ACS Nano* **2020**, 14, 2904.
- [7] a) Z. Yuan, K. Zhang, X. Jiao, Y. Cheng, Y. Zhang, P. Zhang, X. Zhang, Y. Wen, *Biomater. Sci.* **2019**, 7, 5084; b) J. Liu, T. Li, H. Zhang, W. Zhao, L. Qu, S. Chen, S. Wu, *Mater. Today Bio* **2022**, 14, 100243.
- [8] a) L. i-S. Lin, T. Huang, J. Song, X.-Y. u Ou, Z. Wang, H. Deng, R. Tian, Y. Liu, J.-F. Wang, Y. Liu, G. Yu, Z. Zhou, S. Wang, G. Niu, H.-H. Yang, X. Chen, *J. Am. Chem. Soc.* **2019**, 141, 9937; b) R. Zhang, G. Jiang, Q. Gao, X. Wang, Y. Wang, X. Xu, W. Yan, H. Shen, *Nanoscale* **2021**, 13, 15937.

- [9] a) H. Yuan, P. Xia, X. Sun, J. Ma, X. Xu, C. Fu, H. Zhou, Y. Guan, Z. Li, S. Zhao, H. Wang, L. Dai, C. Xu, S. Dong, Q. Geng, Z. Li, J. Wang, *Small* **2022**, *18*, 2202161; b) X. He, M. Li, S. Fan, Y. Li, L. Fang, G. Xiang, *Chem. Eng. J.* **2024**, *481*, 148522; c) J. E. Cun, Z. He, X. Fan, Q. Pan, K. Luo, B. He, Y. Pu, *Small* **2025**, *21*, 2409875.
- [10] a) S. R. Park, Y. J. Yoo, Y. H. Ban, Y. J. Yoon, *J. Antibiot.* **2010**, *63*, 434; b) D. Benjamin, M. Colombi, C. Moroni, M. N. Hall, *Nat. Rev. Drug Discovery* **2011**, *10*, 868.
- [11] a) M. Chang, Z. Hou, M. Wang, P. Dang, J. Liu, M. Shu, B. Ding, A. A. Al Kheraif, C. Li, J. Lin, *Small* **2020**, *16*, 1907146; b) L. Liu, H. Zhang, S. Xing, Y. Zhang, L. Shanguan, C. Wei, F. Peng, X. Liu, *Adv. Sci.* **2023**, *10*, 2207342; c) X. Jiang, S. Zhang, F. Ren, L. Chen, J. Zeng, M. Zhu, Z. Cheng, M. Gao, Z. Li, *ACS Nano* **2017**, *11*, 5633.
- [12] a) Y. Du, M. Yu, J. Ge, P. X. Ma, X. Chen, B. Lei, *Adv. Funct. Mater.* **2015**, *25*, 5016; b) M. Yang, Y. Guo, M. Yu, P. X. Ma, C. Mao, B. Lei, *Acta Biomater.* **2017**, *54*, 69; c) L. Zhu, Y. Zhang, Y. Ji, *J. Mater. Sci. Mater. Med.* **2017**, *28*, 93.
- [13] Y. Guo, K. Liang, Y. Ji, *Eur. Polym. J.* **2019**, *110*, 337.
- [14] T. J. Rivers, T. W. Hudson, C. E. Schmidt, *Adv. Funct. Mater.* **2002**, *12*, 33.
- [15] A. Salam, M. Q. Khan, T. Hassan, N. Hassan, A. Nazir, T. Hussain, M. Azeem, I. S. Kim, *Sci. Rep.* **2020**, *10*, 19751.
- [16] a) Y. Huangfu, S. Li, L. Deng, J. Zhang, P. Huang, Z. Feng, D. Kong, W. Wang, A. Dong, *ACS Appl. Mater. Interfaces* **2021**, *13*, 59695; b) X. Liu, L. Gao, S. Fu, W. Zhao, F. Wang, J. Gao, C. Li, H. Wu, L. u Wang, *Mater. Des.* **2023**, *227*, 111706.
- [17] R. Xu, H. Xia, W. He, Z. Li, J. Zhao, B. o Liu, Y. Wang, Q. Lei, Y. i Kong, Y. Bai, Z. Yao, R. Yan, H. Li, R. Zhan, S. Yang, G. Luo, J. Wu, *Sci. Rep.* **2016**, *6*, 24596.
- [18] Z. Ujang, A. H. A. Rashid, S. K. Suboh, A. S. Halim, C. K. Lim, *J. Appl. Biomater. Funct. Mater.* **2014**, *12*, 155.
- [19] E. R. Lorden, K. J. Miller, L. Bashirov, M. M. Ibrahim, E. Hammett, Y. Jung, M. A. Medina, A. Rastegarpour, M. A. Selim, K. W. Leong, H. Levinson, *Biomaterials* **2015**, *43*, 61.
- [20] X. Chen, X. Wang, D. Fang, *Fullerenes, Nanotubes Carbon Nanostruct.* **2020**, *28*, 1048.
- [21] V. Estrella, T. Chen, M. Lloyd, J. Wojtkowiak, H. H. Cornnell, A. Ibrahim-Hashim, K. Bailey, Y. Balagurunathan, J. M. Rothberg, B. F. Sloane, J. Johnson, R. A. Gatenby, R. J. Gillies, *Cancer Res.* **2013**, *73*, 1524.
- [22] Z. Chu, J. Yang, W. Zheng, J. Sun, W. Wang, H. Qian, *Coord. Chem. Rev.* **2023**, *481*, 215049.
- [23] a) B. Liu, Y. Bian, S. Liang, M. Yuan, S. Dong, F. He, S. Gai, P. Yang, Z. Cheng, J. Lin, *ACS Nano* **2022**, *16*, 617; b) G. Getachew, C. Korupalli, A. S. Rasal, J. Y. Chang, *Compos. B Eng.* **2021**, *226*, 109364.
- [24] a) S. Kim, J. H. Seo, D. I. Jeong, M. Yang, S. Y. Lee, J. Lee, H. J. Cho, *Biomater. Sci.* **2021**, *9*, 847; b) S. Kim, Q. Hao, D. I. Jeong, J. W. Huh, Y. E. Choi, H. J. Cho, *Mater. Des.* **2023**, *231*, 112063.
- [25] R. Jiang, X. Li, D. Hu, M. Zhu, D. i Zhou, M. Yuan, X. Hu, S. Nie, J. Liu, H. Xiang, H. Yang, Y. i Zhang, S. Wang, *Appl. Mater. Today* **2021**, *23*, 101066.
- [26] W. F. Song, J. Y. Zeng, P. Ji, Z. Y. Han, Y. X. Sun, X. Z. Zhang, *Small* **2023**, *19*, 2301148.
- [27] a) D. Yamamoto, T. Inui, Y. Tsubota, N. Sueoka, C. Yamamoto, K. Kuwana, M. Yamamoto, *World J. Surg. Oncol.* **2012**, *10*, 201; b) A. Bakker, C. P. Tello Valverde, G. van Tienhoven, M. W. Kolff, H. P. Kok, B. J. Slotman, I. R. H. M. Konings, A. L. Oei, H. S. A. Oldenburg, E. J. T. Rutgers, C. R. N. Rasch, H. J. G. D. van den Bongard, H. Crezee, *Radiother. Oncol.* **2022**, *167*, 149; c) S. Maluta, M. W. Kolff, *Breast Care* **2015**, *10*, 408; d) Y. Yang, L. Huanfu, H. Li, D. Yang, *Int. J. Hyperthermia* **2023**, *40*, 2270654.
- [28] S. Shen, J. Qiu, D. Hui, Y. Xia, *Small* **2023**, *20*, 2305426.
- [29] a) Y. Li, Y. Wang, Y. Ding, X. i Fan, L. Ye, Q. Pan, B. Zhang, P. Li, K. Luo, B. Hu, B. He, Y. Pu, *ACS Nano* **2024**, *18*, 17251; b) X. Yang, C. Zhang, D. Deng, Y. Gu, H. Wang, Q. Zhong, *Small* **2022**, *18*, 2104368.
- [30] D. Y. Kong, J. H. Park, K. W. Lee, H. Park, J. A. Cho, *Biomed. Sci. Lett.* **2016**, *22*, 75.
- [31] C. A. Schneider, W. S. Rasband, K. W. Eliceiri, *Nat. Methods* **2012**, *9*, 671.
- [32] T. C. Türkoğlu, M. Sarıışık, S. Y. Karavana, F. A. Köse, *Carbohydr. Polym.* **2021**, *269*, 118287.
- [33] S. Kim, J.-J. Kim, J.-H. Jeong, Y. Kim, J. Park, D. I. Jeong, H. J. Kim, C. Hwang, S.-H. Ahn, H.-J. Ko, H.-J. Cho, *Mater. Sci. Eng. C* **2021**, *131*, 112537.
- [34] G. Getachew, C. Korupalli, A. S. Rasal, W. B. Dirersa, M. Z. Fahmi, J. Y. Chang, *ACS Appl. Mater. Interfaces* **2022**, *14*, 278.
- [35] a) P. Chen, X. Li, R. Zhang, S. Liu, Y. Xiang, M. Zhang, X. Chen, T. Pan, L. Yan, J. Feng, T. Duan, D. Wang, B. Chen, T. Jin, W. Wang, L. Chen, X. Huang, W. Zhang, Y. Sun, G. Li, L. Kong, X. Chen, Y. Li, Z. Yang, Q. Zhang, L. Zhuo, X. Sui, T. Xie, *Theranostics* **2020**, *10*, 5107; b) Y. Li, X. Wang, J. Yan, Y. u Liu, R. Yang, D. Pan, L. Wang, Y. Xu, X. Li, M. Yang, *Biomater. Sci.* **2019**, *7*, 3779.
- [36] a) D. I. Jeong, S. Kim, S. Y. Lee, H. J. Kim, J. Lee, K. Lee, H. J. Cho, *Chem. Eng. J.* **2022**, *438*, 135584; b) D. I. Jeong, H. J. Kim, S. Y. i Lee, S. Kim, J. W. Huh, J.-H. Ahn, M. Karmakar, H.-J. Kim, K. Lee, J. Lee, H.-J. Ko, H.-J. Cho, *J. Controlled Release* **2024**, *366*, 142.